Article:
Gudmundsson, MT, Jónsdóttir, K, Hooper, A et al. (2016) Gradual caldera collapse at Bárdarbunga volcano, Iceland, regulated by lateral magma outflow. Science, 353 (6296). aaf8988. ISSN: 0036-8075

https://doi.org/10.1126/science.aaf8988

Gradual caldera collapse at Bárdarbunga volcano, Iceland, regulated by lateral magma outflow

Magnús T. Gudmundsson[1], Kristín Jónsdóttir[2], Andrew Hooper[3], Eoghan P. Holohan[4,5], Saemundur A. Halldórsson[1], Benedikt G. Ófeigsson[2], Simone Cesca[4], Kristín S. Vogfjörd[2], Freysteinn Sigmundsson[1], Thórdís Högnadóttir[1], Páll Einarsson[1], Olgeir Sigmarsson[1,6], Alexander H. Jarosch[1], Kristján Jónasson[7], Eyjólfur Magnússon[1], Sigrún Hreinsdóttir[8], Marco Bagnardi[3], Michelle M. Parks[1], Vala Hjörleifsdóttir[9], Finnur Pálsson[1], Thomas R. Walter[4], Martin P.J. Schöpfer[10], Sebastian Heimann[4], Hannah I. Reynolds[1], Stéphanie Dumont[1], Eniko Bali[1], Gudmundur H. Gudfinnsson[1], Torsten Dahm[4], Matthew Roberts[2], Martin Hensch[2], Joaquín, M.C. Belart[1], Karsten Spaans[3], Sigurdur Jakobsson[1], Gunnar B. Gudmundsson[2], Hildur M. Fridriksdóttir[1,2], Vincent Drouin[1], Tobias Dürig[1], Gudfinna Adalgeirsdóttir[1], Morten S. Riishuus[1], Gro B.M. Pedersen[1], Tayo van Boeckel[1] , Björn Oddsson[11], Melissa A. Pfeffer[2], Sara Barsotti[2], Baldur Bergsson[2], Amy Donovan[12], Mike R. Burton[13], Alessandro Aiuppa[14]

Revised manuscript for Science – 14 June 2016

1: Nordvulk, Institute of Earth Sciences, University of Iceland, Sturlugata 7, 101 Reykjavík

2: Icelandic Meteorological Office, IS-150 Reykjavík, Iceland

3: Centre for the Observation and Modelling of Earthquakes, Volcanoes *and Tectonics (COMET), School of Earth and Environment, University of Leeds, Leeds LS2 9JT, UK*

4: GFZ German Research Centre for Geosciences, Telegrafenberg, 14473 Potsdam, Germany

5: UCD School of Earth Sciences, University College Dublin, Ireland

6: Laboratoire Magmas et Volcans, CNRS-Université Blaise Pascal-IRD, 63038 Clermont-Ferrand, France

7: Faculty of Industrial and Mechanical Engineering and Computer Science, University of Iceland, Hjarðarhagi 2-6, 107 Reykjavík, Iceland

8: GNS Science, PO Box 30368, Lower Hutt 5040, New Zealand

9: Departamento de Sismología, Instituto de Geofísica, Universidad Nacional Autónoma de Mexico, 04510 Ciudad de México, Mexico

10: Department for Geodynamics and Sedimentology, University of Vienna, Althanstrasse 14, A-1090 Vienna, Austria.

11: National Commissioner of the Icelandic Police, Department of Civil Protection and Emergency Management, Skúlagata 21, 101 Reykjavík, Iceland

12: King's College London, King's Building, Strand Campus, London WC2R 2LS, England, United Kingdom

13: University of Manchester, Williamson Building, Oxford Road, Manchester, M13 9PL, UK

14: University of Palermo – Piazza Marina, 61 90133, Palermo, Italy

Abstract

Large volcanic eruptions on Earth commonly occur with collapse of the roof of a crustal magma reservoir, forming a caldera. Only a few such collapses occur per century and lack of detailed observations has obscured insight on mechanical interplay between collapse and eruption. We use multi-parameter geophysical and geochemical data to show that the 110 km^2 and 65 m deep collapse of Bárdarbunga caldera in 2014-15 initiated through withdrawal of magma, and lateral migration through a 47 km long dyke, from a 12 km deep reservoir. Interaction between the pressure exerted by the subsiding reservoir roof and the physical properties of the subsurface flow path explain the gradual, near exponential decline of both collapse rate and the intensity of the 181-day long eruption.

Calderas are 1 - 100 km diameter depressions found in volcanic regions of Earth and other planets. They mainly form by collapse of overburden into a subterranean magma reservoir during large volcanic eruptions, including the largest known super-eruptions (*1*-*8*). From 1900 AD to 2014, only six cases have been documented and with varying degrees of detail. The collapses of Katmai in 1912 and Pinatubo in 1991 occurred during explosive silicic (andesite-rhyolite) eruptions, the largest of the 20th century. The collapses of Fernandina in 1968, Tolbachik in 1975-76, Miyakejima in 2000 and Piton de la Fournaise in 2007 were associated with mainly effusive mafic (basalt – basaltic andesite) intrusive activity and eruptions (*2*, *9*-*12*).

The consensus from field and modelling studies is that caldera collapse progresses from initial surface downsag to fault-controlled subsidence (*1*, *8*, *13*, *14*). The limited number of modern examples and the scarcity of geophysical data leaves open the question of whether collapse occurs suddenly or gradually during the course of an eruption. The issue of whether collapse drives magma movement and eruption or eruption drives collapse also remains unresolved. Previous geological,

geophysical, and modeling studies have produced a diverse and inconsistent set of answers to such questions (*2*, *4*, *15*, *16*). The caldera collapse at Bárdarbunga in central Iceland from August 2014 to February 2015 offers a unique opportunity to address them directly.

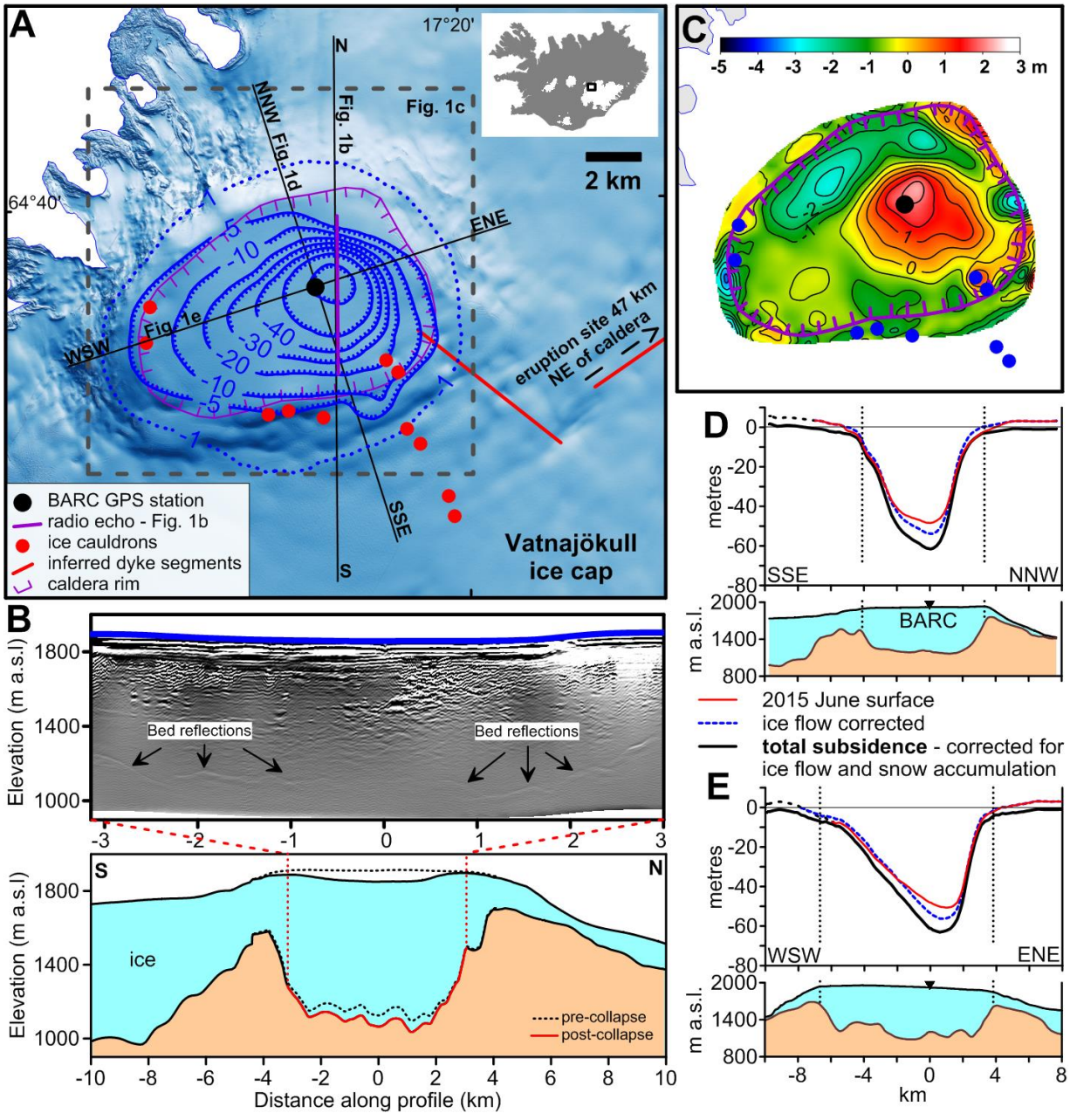

Figure 1. Bárdarbunga and geometry of collapse. A) Map showing the total caldera subsidence (in meters) at the end of collapse in February 2015þ Minor sustained geothermal activity, monitored from aircraft, increased during the collapse with pre-existing ice cauldrons deepening by up to 50 m and new ones forming at the southern margin and to the southeast of the caldera (*24*). (B) Radio-echo sounding profile from 3 February, 2015, and a cross-section of the caldera with the collapse.

The pre-collapse topography is obtained by subtracting the subsidence observed at the surface. (C) Modelled changes in ice thickness at the end of February 2015 resulting from ice flow in response to caldera collapse (*24*). D) NNW-SSE and E) WSW-ESE cross-sections as measured in June 2015, corrected for winter snow accumulation in 2014-15, measured in June 2015, and modeled vertical ice flow. Subsidence extends 2-3 km beyond the pre-existing caldera rims (dotted lines) where it amounts to 3-11 m.

The Bárdarbunga volcano and the Holuhraun eruption of 2014-15

Bárdarbunga volcano (Fig. 1) and its related fissure swarms form a 150 km long volcanic system on the boundary between the North-American and Eurasian tectonic plates. The volcano resides beneath the Vatnajökull ice cap and has a broadly elliptic 13 by 8 km wide and 500-700 m deep caldera with a long axis trending ENE. About 700-800 m of ice fills the caldera (*17*, *18*). Over 20 eruptions have occurred on the fissure swarms outside the caldera in the last 12 centuries, including three that produced 1-4 km^3 of magma, but no eruptions are known within the caldera in this period. (*19*).

At 4 UTC on 16 August 2014, the onset of intense seismicity beneath the caldera marked the beginning of a major rifting event (*20*). The seismic activity was mostly located in the SE-corner of the caldera in the first few hours, but it soon began to propagate out of the caldera towards the SE (Fig. 2). After propagating to about 7 km from the caldera rim, fifteen hours after the onset of seismicity (~19 UTC), the moving earthquake cluster took a 90° turn and started migrating towards the NE. In the two weeks that followed, surface deformation and migration of seismicity indicated that a magmatic dike propagated laterally northeastward for 47 km in the uppermost 6-10 km of the Earth's crust (*20*, *21*). On 31 August, a major effusive eruption began above the far end of the dike; this lasted six months and produced 1.5±0.2 km^3 of lava (~1.4±0.2 km^3 of bubble-free magma) (*22*), making it the largest in Iceland (or Europe) since the 1783-84 Laki eruption. Combined with

98 the 0.5±0.1 km^3 dyke (*20*), the total volume of identified intruded and erupted magma was 1.9±0.3
99 km^3.

100 **The Onset of Collapse**

101 After the initial seismic activity in the caldera receded late on 16 August, seismicity was relatively
102 minor there until 20 August. At the same time our GPS time-series from stations close to the
103 caldera, suggest that deflation of the magma reservoir started on 16 August (*20*). On 20 August,
104 caldera seismicity increased progressively with a series of earthquakes of magnitude M4-M5.8
105 occurring in the following days (Fig. 2). The first two events occurred on the southern caldera rim
106 (M4.7 on 20 August and M5.1 on 21 August). Following these earthquakes, three similar magnitude
107 events occurred on the northern rim on 23 August, followed by four events on the southern rim on
108 24-25 August. On 26 August activity shifted again to the northern rim with a M5.8 earthquake, the
109 largest in the whole series. These data indicate that significant movement on ring faults started on
110 the south side with the 20-21 August earthquakes, then began on the north side on 23 August, and
111 by 24 August the ring faults on both sides where slipping, a process that did not terminate until at
112 the end of February. Onset of collapse therefore likely occurred on 20 August with the ring fault
113 fully activated on 24 August. If we compare the evolution of the dike together with the seismic
114 moment release of the caldera collapse earthquakes, we can clearly see that the dike migration leads
115 the moment release curve (Fig. 2A). We therefore conclude that onset of collapse resulted from a
116 pressure drop in the reservoir as magma was laterally withdrawn into the propagating dike, with the
117 latter possibly primarily driven by regional tectonic tensional stresses (*20*).

118 The volume of the expanding dike on 20 August had reached approximately 0.25 km^3, increasing to
119 0.35 km^3 on 24 August (*20*) with the source of this magma being the reservoir beneath the caldera.
120 The relatively minor caldera seismicity on 17-19 August indicates the material overlying the
121 magma reservoir deformed mostly elastically until it reached a critical failure point of caldera
122 collapse on 20-24 August. If we assume that the entire volume of eruptible magma within the

reservoir was 1.9±0.2 km^3, then the critical volume fraction required to reach the failure point and trigger the collapse (*23*) was 0.12-0.21.

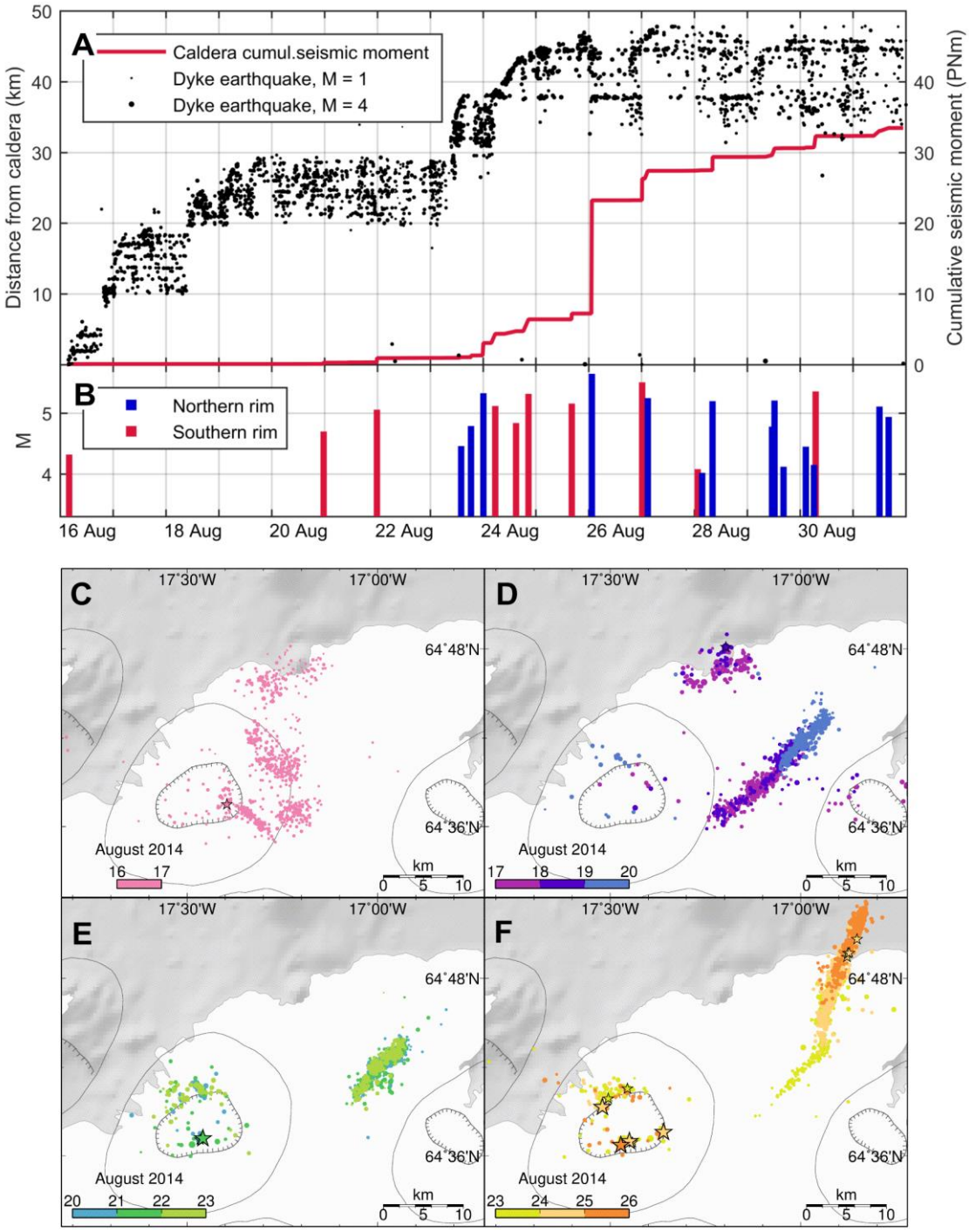

Figure 2. Onset of caldera collapse. A) Cumulative seismic moment release from caldera earthquakes plotted together with distribution of seismicity along the dike length, using high quality

relative locations of earthquakes (*20*), for the time period when the dike progressed away from the caldera. B) Significant caldera earthquakes with magnitudes above M4 plotted as impulses, where the height represents magnitude and color represents location on southern or northern rim. C) Map of NW Vatnajökull showing earthquake epicenters on 16 August, D) 17-19 August, E) 20-22 August and F) 23-15 August.

Ice Flow, Subsidence Magnitude and Volume

As we recorded the caldera subsidence mainly on the ice (Fig. 1, Fig. S1), we made corrections and additional measurements to derive the underlying bedrock displacement. Our main data on ice surface changes and ice movements are repeated C-band radar altimeter surveys from aircraft, maps made from optical satellite images and the continuously recording GPS station BARC we set up in the center of the caldera on 13 September. The observed velocities and displacements of the ice surface are displayed on Figs. 3A and 3B. We use these observations to constrain three-dimensional Full-Stokes finite element modelling of ice-flow in response to the collapse (*24*). The results show concentric flow, towards the point of maximum collapse within the caldera, with maximum ice thickening at the center of ~3 m by February 2015 (Fig. 1C, Fig. S2). The maximum ice surface lowering of 62±2 m, determined by aerial altimeter surveys, gives a maximum bedrock subsidence of 65±3 m. Our data and models show that apart from the concentric flow towards the deepest part of the subsidence (about 1 km east of BARC) horizontal flow was not much affected (Fig. 3A). We therefore conclude that suggestions of a large increase in ice flow out of the caldera during these events (*25*) cannot be fitted with our data.

Bedrock subsidence exceeding 1 m occurred within an area of 110 km^2 that extended beyond the pre-existing caldera (Fig. 1, Fig. S1). After termination of collapse the total subsidence at the pre-existing caldera rims amounted to 3 to 11 meters (Fig. 1D and 1E). Using subglacial radio-echo soundings we observed a down-sagged bedrock surface without any clear signs of fault offset (Fig 1B) or indications of water bodies at the ice bedrock interface. The limited resolution resulting

154 from the 600-800 m ice thickness means that we cannot on the basis of the radio-echo results
155 exclude the possibility of steep fault escarpments. However, substantial vertical fault movement at
156 the base of the glacier would result in high strain rates within the basal ice which would instantly
157 fracture the ice fabric and propagate upward. During drainage of subglacial lakes in Iceland, large
158 surface fractures induced by basal motion have been observed repeatedly (*26*) and can serve here as
159 an analog for the possible surface manifestations of vertical basal motion. The absence of such
160 surface ice fractures at Bárdabunga indicates that no substantial fault escarpment formed at the
161 bottom. The calculated collapse volume is 1.8±0.2 km^3, not significantly different from the
162 combined volume of erupted and intruded magma (Fig. 3B).

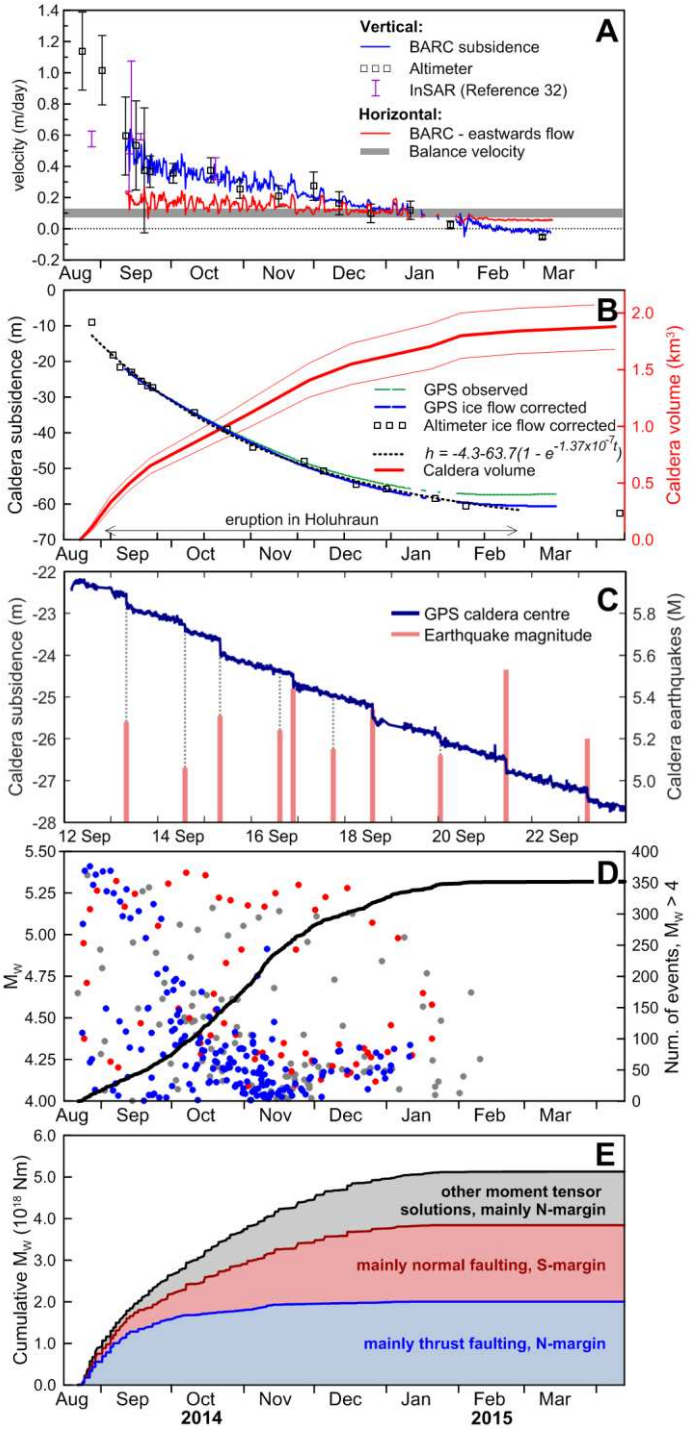

Figure 3. Time series of collapse. A) Vertical and horizontal velocities measured at the BARC GPS station in the center of the caldera (Fig. 1A), including the rate of vertical rate of ice surface subsidence found from altimeter aircraft data and optical satellite photogrammetry. The balance velocity is obtained by estimating the rate of displacement required to transport the net accumulation of the area draining ice towards east in the western part of the caldera. InSAR derived vertical velocities are based on (*32*). B) Subsidence at the center of the caldera and

subsidence volume evolution. The volume of the subsidence is obtained by subtracting the mapped surface from the pre-collapse surface. The caldera subsidence curve is fitted with an equation of the same form as eq. (1). C) High resolution GPS for 12-23 September, showing M>5 earthquakes coinciding with 20-40 cm rapid collapse, superimposed on gradual subsidence. Note that the size of the steps depends on the location of BARC relative to the earthquake centroids, and cannot be used directly to infer the proportion of ring fault slip that ruptured seismically or aseismically. D) Cumulative number of M>4 caldera earthquakes, with magnitude evolution colored in red, blue and grey representing clusters on the southern rim, the northern rim and smaller clusters, respectively (see Fig. S5). E) Cumulative seismic moment for M>4 caldera earthquakes.

Magma source depth

Lava chemistry, surface gas composition and geodetic modelling indicate drainage of a magma reservoir at a depth of ~12 km. The erupted lava is typical olivine tholeiite with a relatively uniform chemical composition, consistent with efficient homogenization of melts before eruption. Several independent geobarometers (Fig. 4) yield an equilibrium pressure of 350-550 MPa, indicating that melt resided at depths of 11-16 km before the eruption. We obtained a similar result (14±3 km) from analysis of subaerial gas measurements (Fig. 4). This depth concurs with our regional geodetic observations, which are dominated by a deflating source at 8-12 km depth beneath Bárdarbunga, after the cessation of dike-related deformation in mid-September (Figs. S3 and S4).

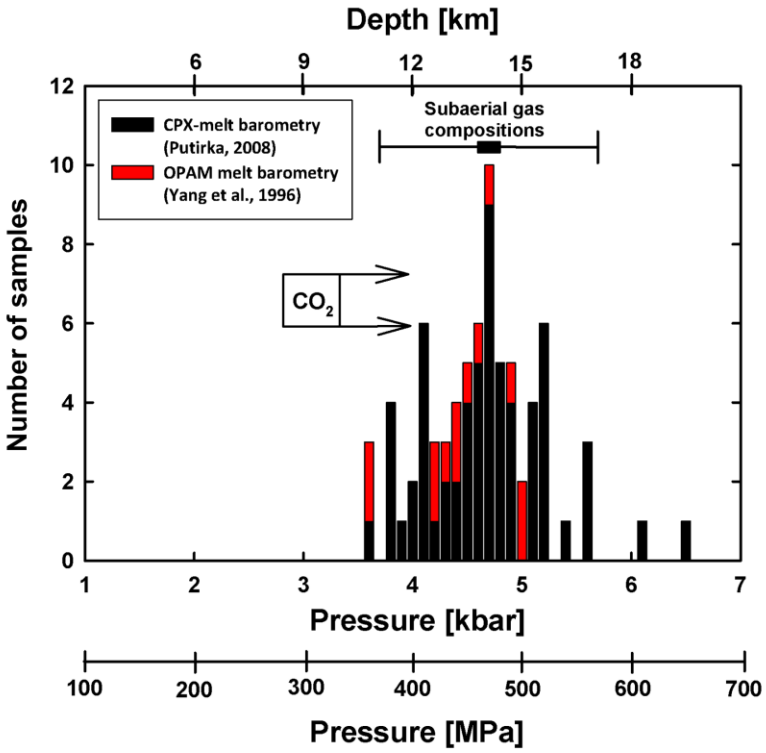

Figure 4. Magma source depth from geobarometric and subaerial gas analysis. The CO2-box indicates the minimum pressure obtained (400 kbar) from density barometry of plagioclase hosted CO2-bearing fluid inclusions. The results from the analysis of subaerial gas compositions are based on FTIR and Multi-GAS measurements (*24*).

Seismicity and subsurface structure

We used seismic data and Distinct Element Method (DEM) numerical modelling (*24*), to characterize the deeper collapse structure as the reactivation of a steeply-inclined ring fault (Fig. 5). We mostly observed seismicity at depths of 0-9 km beneath the northern and southern caldera rims (Fig. 5B), with earthquakes being more numerous on the northern rim. This spatial pattern of seismicity is consistent with fracturing above a deflating magma reservoir that was elliptical in plan-view (*27*). In cross-section, the hypocenters indicate a steeply (~80°) outwards-dipping fault in the northern cluster, while the southern cluster they indicate a vertical or near-vertical fault dip. A series of DEM forward simulations of a magma chamber and ring fault system, as constrained by

the hypocenter distribution and by the geobarometry data, tested the above structural interpretation against the observed NNW-SSE subsidence profile. The models indicate that a pre-existing and relatively low friction (coefficient of 0.1-0.2) ring-fault system controlled the subsidence at depth (Fig. 5C, D). Our best fitting models had preexisting faults dipping out at 80-85° from the caldera center on the north side and at 85-90° toward the caldera center on the south side. The modeled pre-existing faults lay at 1-2 km below the surface on the north side and 3-4 km on the south side. Modeling of a more complex fault geometry or the inclusion of greater material heterogeneity may further improve the data fit, but presently lacks robust geophysical constraints. The arrangement of an outward dipping fault on one side of a caldera and an inward-dipping fault on the other is typical of 'asymmetric' or 'trapdoor-like' collapses produced in past analog and numerical modeling studies (*8*, *28*, *29*). It also occurs at Glencoe (*29*) and Tendurek (*30*) volcanoes . Finally, our finding is consistent with past seismological results that defined a very similar ring-fault geometry during the last period of activity at Bardarbunga in 1996 (*31*).

Through regional moment tensor (MT) inversion, we infer that the source mechanisms of 77 M>5 events (Fig. S5) confined to two clusters beneath the northern and southern rim regions show contributions of both shear and non-shear components. The shear components indicate possible ruptures of segments on the ring fault. Shear failure on inward dipping ring faults, or the sudden injection of magma in horizontal fissures forming sills have been proposed (*32*) to explain the shear components of the observed earthquakes at Bárdarbunga. We, however, narrowed down on plausible solutions by using the micro-earthquakes (Fig. 5A). The moment tensor solutions are well constrained, but the inferred dip of the shear plane we obtain is uncertain since the non-shear component, in this case a negative, sub-vertical compensated linear vector dipole (vCLVD), is dominant. As a result, the shear orientation obtained depends very much on the decomposition approach.

By using the constraint of the steeply outward dipping ring fault on the northern cluster we derive a MT solution that is a combination of a negative vCLVD and steep E-W striking reverse faulting

(Fig. 3D, 3E and Fig. S5). In contrast, standard decomposition of the northern cluster MTs provides normal faulting along steep N-S striking planes, a result that is inconsistent with the observed main fault orientation. The southern cluster MTs are consistent with being composed of families (*33*) of steep normal faulting earthquakes.

The large, negative vCLVD indicates a combination of downward contraction and horizontal expansion, as has been observed in mines as well as in volcanic calderas during collapses (e.g. *31*, *34*). This could imply failure of support structures directly above or even within the magmatic reservoir, or the sudden response of the reservoir fluid to vertical compression.

Temporal development of subsidence and related seismicity

Subsidence occurred gradually during the eruption (Fig. 3B). From an initial rate in the caldera center of ~1 m/day during the first 20 days (Fig. 3B), subsidence declined in a near exponential manner with time (24). Subsidence terminated when the eruption ended in February 2015. We can associate some of the M>5 caldera earthquakes, during the first couple of months of activity, with drops of 10-40 cm, but subsidence was otherwise continuous (Fig. 3C). The gradual decline in the rates of subsidence and caldera volume growth is mirrored by a decline in the cumulative seismic moment, the latter reflecting a decrease in the number of larger earthquakes with time (Fig. 3D, 3E). Nonetheless, in terms of the cumulative seismic moment of 5.07×10^{18} Nm for the M>4.0 events, this collapse is the second largest recorded, after that of Katmai (1912) (*35*). The geodetic moment depends on the shear modulus, the fault area and the amount of slip assumed. The shear modulus could be very low in regions of intense faulting such as on a caldera ring fault. The possible range of the geodetic moment is found by considering a ring fault reaching from the surface to 12 km depth, 60 m of slip and a shear modulus over a wide range, 2-20 GPa. This results in a moment of 4×10^{19} - 4×10^{20} Nm, or 10-100 times the cumulative seismic moment of the earthquakes. This difference is consistent with the modeling of surface deformation observed during one of the events (Fig S7).

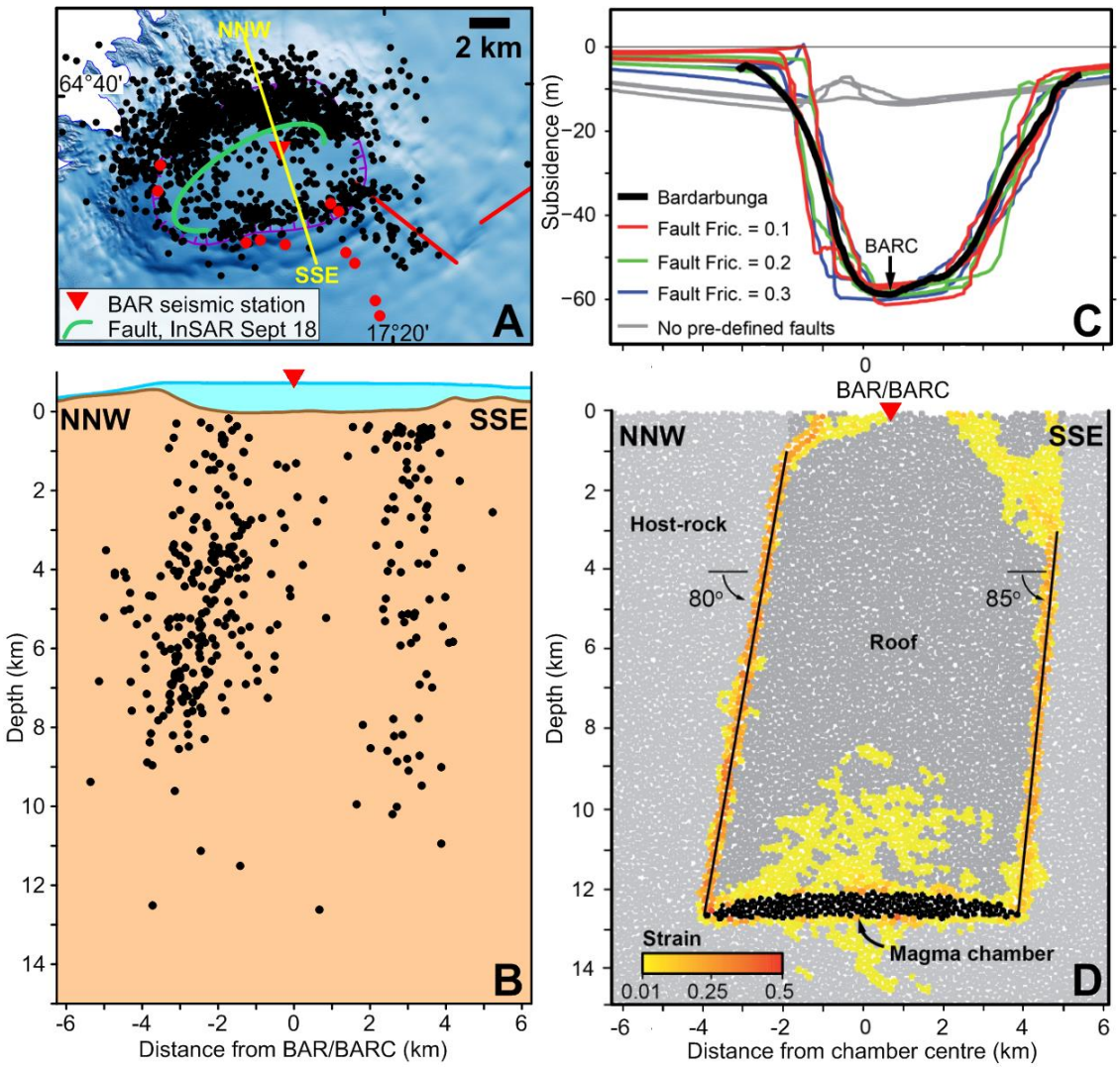

255

256 **Figure 5: Fault geometry and collapse modelling:** A) Earthquakes 1 August – 17 October 2014,
257 B) seismicity along a 2-4 km wide strip on the NNW-SSE cross section, depth relative to bedrock
258 caldera floor. C-D) Two-dimensional DEM modeling of the collapse, constrained by subsidence
259 geometry, earthquake locations in (B), and the geobarometry (Fig. 4). The geometry illustrated in
260 (D) obtained the best agreement with the observations. The color scale shows the maximum finite
261 shear strain. Surface displacement profiles for different pre-existing fault frictions are provided in
262 (C). Three model realizations are shown for each friction value.

Caldera-flowpath interaction and piston collapse modeling

We see a short-term (multi-hourly) mechanical coupling of the collapsing caldera and the distal dike (south of eruption site) in the timing of earthquakes in the dike and at the caldera (Fig. 6A). Within a six-hour window before and after large caldera earthquakes the frequency of dike earthquakes was increased relative to background rate (24). We observed this pattern in the data after the beginning of October 2014, when the dyke had stopped propagating and a quasi-steady magma flow path had developed, until February 2015 when seismic activity stopped. For the three hours after caldera earthquakes with magnitude $M > 4.6$, as well as for the three hours before caldera earthquakes with $M > 4.0$, the increase in seismicity was significant (*24*) ($p = 0.05$; Fig. 6, Fig. S8).

At Bárdarbunga communication therefore existed between caldera subsidence events and pressure changes in a conduit up to 47 km away. Spatiotemporal patterns of tilt at Kilauea Volcano, Hawaii, show a similar phenomenon that can be explained by the propagation of pressure transients within an elastically deformable dyke (*36*). By analogy, we can make the interpretation that caldera earthquakes may generate a pressure pulse that leads to increased seismicity at the end of the dike. The communication could be two-way, although it is difficult to explain a pressure pulse from the dike towards the caldera. One possibility is that readjustment of the dike (e.g. sudden unblocking) can increase the dike volume slightly and subsequently lower the magma pressure which then translates back to the caldera. The communication may also be entirely one-way, from the caldera to the dike: smaller caldera earthquakes, and/or aseismic deformation at depth just above the magma chamber may precede a large caldera earthquake, increasing dike pressure and dike seismicity.

We explain the longer term (weeks to months scale) coupling in the form of the gradually declining rates of caldera subsidence, caldera volume change and lava eruption (Figs. 3B, 6B) with a model of a collapsing piston overlying a pressurized magma chamber. We assume that the chamber pressure and fault friction each partially support the piston weight (*24*). Drainage of magma reduces

288 the chamber pressure and causes piston subsidence (Fig. S6). This in turn raises the chamber
289 pressure, leading to a feedback loop that maintains quasi-constant pressure at the magma chamber
290 top, and drives further magma drainage. The pressure feeding the eruption drops, however, due to
291 the reduction in hydraulic head of magma over time. Kumagai et al. (37) also used a piston model to
292 explain caldera collapse at Miyakejima in 2000, but in their model no change in hydraulic head was
293 assumed and outflow rate was held constant.

294 Assuming that the time-averaged resistive force due to friction on the ring faults remains constant,
295 and that magma flow is laminar through a cylindrical pipe with radius r, and conduit length L, with
296 L>>r, then

297 $$\Delta P \approx \Delta P_0 e^{-\frac{\pi \rho g r^4}{8 A \eta L} t} \quad (1)$$

298 Where ΔP is the driving overpressure, ΔP_0 is the initial driving overpressure, ρ is the density of the
299 magma, g is gravitational acceleration, A is the cross-sectional area of the magma chamber, η is the
300 dynamic viscosity of the magma and t is time (*24*). We estimated ΔP_0 and the constant in the
301 exponent, assuming that the measured subsidence within the caldera represents the decrease in
302 magma chamber height with time (Fig 3B). Note, this represents a minimum estimate for ΔP_0, as
303 there may also have been dilation at depth. The model also fits the measured caldera volume
304 change (Fig. 3B) and eruption rate (Fig. 6B). This model predicts the same form of decay in flow
305 rate (exponential) as the standard 'Wadge' model of depressurisation of an overpressured magma
306 body (*38*), but by a different mechanism. The feedback mechanism of re-pressurisation from the
307 ongoing piston collapse enhanced the length and speed of dike propagation, and the duration of the
308 eruption. In this model, therefore, both the eruption drives the collapse and collapse drives the
309 eruption.

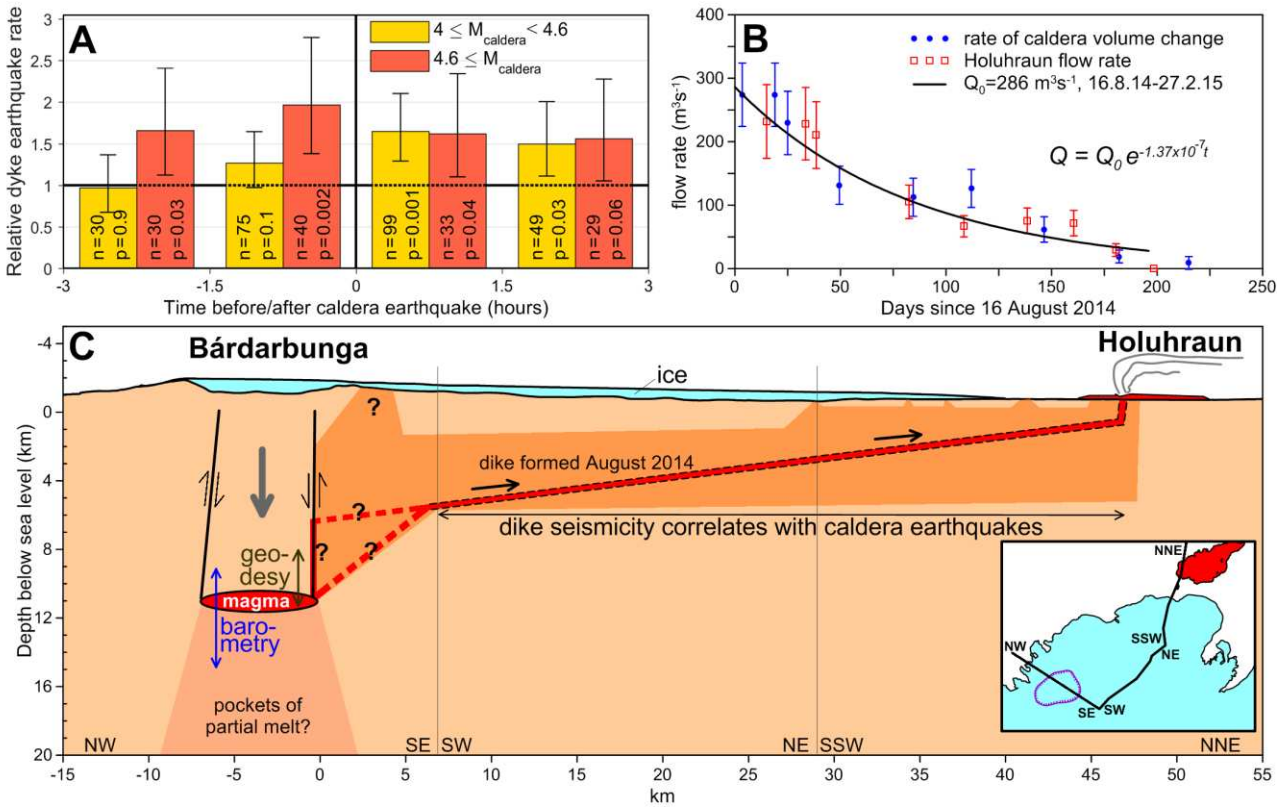

Figure 6. Caldera - magma flowpath interaction. A) Rate of dike earthquakes relative to background levels before and after significant caldera earthquakes of magnitude >M4. The p-values indicate the two sided significance and n is the number of earthquakes used. Error bars indicate 90% confidence intervals (24). B) Exponential model of magma flow rate constrained by caldera GPS subsidence (*24*) compared with rate of volume change in caldera and eruption rate in Holuhraun. The eruption stopped on Day 194 (27 February, 2015) before the driving pressure reaches zero, as expected if the conduit becomes clogged by solidifying magma as the flow rate drops. C) Schematic cross-section of caldera - magma chamber - pipe-like magma flow path and eruption site after dike formation (*20*, *21*). The inferred magma chamber is set at 12 km below bedrock caldera floor. It is possible that magma ascended first along the ring fault before forming the dyke above 6-10 km depth. We indicate the constraints on depth to magma chamber from geobarometry with a blue arrow and from geodesy with a green arrow.

Overview and implications

Table 1 contextualizes the key features of the 2014-15 Bardarbunga collapse with respect to those of the seven collapses instrumentally monitored to date. The areal extent of the Bardarbunga collapse (110 km^2) is the largest yet observed historically and is comparable to that associated with major silicic eruptions in the geological record (6). The total subsidence (65 m) is one to two orders of magnitude smaller than all past collapses listed here, but the large area means that it has the fourth largest collapse volume (1.8 km^3) overall. The erupted volume (1.4 km^3) is the largest of the observed mafic collapses so far, although considerable uncertainty surrounds the volumes associated with the collapse of Fernandina. In volume terms, both the silicic eruptions and collapses of Katmai and Pinatubo were twice to six times larger. The cumulative seismic energy release at Bardarbunga (25 x 10^{13} J, see Table 1) is dwarfed by that of Katmai (1600 x 10^{13} J) and similar to Miyakejima (22 x 10^{13} J), despite the much smaller area of the latter (1.9 km^2). This is explained by the much greater subsidence at Miyakejima (>1600 m). The gradual collapse of Bardarbunga had the second longest duration (190 days) yet recorded. Only the duration of collapse at Tolbachik (515 days) exceeds it. Finally, Bardarbunga has the longest confirmed length of an associated lateral intrusion (48 km) and the longest distance to the main vent (40 km).

Volcano	Year	Magma	Maximum subsidence (m)	Collapse Duration (days)	Collapse Area (km^2)	Collapse Volume (km^3)	Reservoir Depth (km)	Intrusion Volume (km^3) [a]	Erupted Volume (km^3) [b]	Total Magma Volume (km^3)	Distance to Vent [c] (km)	Intrusion Length [d] (km)	Seismic Energy (x 10^{13} J) [e]	Max. EQ [f]
Bardarbunga	2015	Basalt	~ 61	150	110	1.8	11-16	0.5	1.5	2	46	48	25	5.4
La Reunion	2007	Basalt	~ 450	2	0.82	0.1	2-3	0.02	0.14	0.16	7	7	?	3.2
Miyakejima	2000	Basalt	***~ 1600***	40	1.9	0.6	4-7	1.2	0.01	1.21	5.6	35	22	5.6
Tolbachik	1976	Basalt	> 500	**515**	2.5	0.35	4-6?	?	1.2	> 1.2	28	~ 45	?	2.9
Fernandina	1969	Basalt	~ 350	12	7	2	?	?	0.2	> 0.2	10.5?	10.5?	2	5.2
Katmai	1912	Rhyolite	> 1300	3	8.8	***5.5***	2-5	?	*13.5*	*> 13.5*	10	10	*1600*	*7*
*Pinatubo**	*1991*	*Dacite*	*~ 900*	*2*	*4*	*2*	*7-11*	*?*	*4.5*	*4.5*	*1*	*4*	*2*	*5.7*

Table 1: Instrumentally-monitored caldera collapses since 1900 AD.

* Note that all caldera collapses except Pinatubo formed in association with lateral withdrawal and intrusion of magma.

References for data: ***Bardarbunga:*** (*20*); this study; ***La Reunion:*** (*12,16,44-46*); ***Miyakejima:*** (*2, 11, 34, 47-49*); ***Tolbachik:*** (*50-53*); ***Fernandina:*** (*2, 9, 54*); ***Katmai:*** (*35, 41, 55*); ***Pinatubo:*** (*2, 15, 42, 43, 56*)

[a] Intrusion volume values are typically constrained by inversions of data from geodetic networks, and so are available only for the most recent events.

[b] Erupted volumes are given as Dense Rock Equivalent (DRE) – i.e. with porosity removed.

[c] Distance measured from center of caldera to most distant known vent active during collapse.

[d] Estimated horizontal length of the intrusion, from locations of seismicity and/or inversions of geodetic data in all cases except Katmai. For Katmai and Fernandina, intrusion length is estimated as the distance from caldera to vent and is hence a minimum value.

[e] Cumulative seismic energy release calculated by converting the cumulative scalar moments (M_0) by using a factor of $5x10^{-5}$ (from energy-moment relationship determined by Kanamori et al. (*57*))

[f] Maximum earthquake magnitude associated with caldera formation. Magnitude determined from surface waves, Ms, is given for Tolbachik (*53*), Katmai (*35*) and Fernandina (*54*). For La Reunion, M_d is used (*12*, *44*). For Miyakejima and Bardarbunga, the maximum moment magnitude (M_w) for collapse-related VLP events is given (*34*, *58*, this study).

Our data and modelling show that withdrawal and eruption of magma triggered the collapse at Bardarbunga. For the likely depth to diameter ratio of the magma reservoir, the critical volume fraction required to trigger the onset of collapse (0.12-0.21) was much lower than that predicted by past analytical and analogue modelling (*23*, *39*). A similar inference of low critical volume fractions at La Reunion and Miyakejima (*16*) was explained as a consequence of the reactivation of pre-existing ring faults, a proposition in line with our observations and analysis of the Bardarbunga collapse.

Nonetheless, we also show that there is a tight mechanical interplay between collapse and eruption throughout the process once collapse has started, with eruption driving collapse and vice versa on both hourly and eruption-long time scales. For the longer time-scale coupling, the results also show that the physical properties of both the magma chamber roof and the magma pathway regulate caldera collapse and magma outflow rate. Consequently, collapse at Bárdarbunga occurred gradually and at a steadily (exponentially) declining rate. This is a very similar pattern to that inferred for the 1968 Fernandina collapse (*2*, *16*). In contrast to some model predictions (*40*) and to

373 the 2007 collapse of Piton de la Fournaise (*16*), we found no evidence for rapid and sustained
374 pressure increase in the magma chamber as a result of collapse, possibly due to substantial ductile
375 behavior of the roof of the larger and deeper Bardarbunga magma chamber (*13*, *16*).

376 The question of whether or to what extent our understanding of caldera collapse at mafic volcanoes
377 such as Bardarbunga is transferrable to large silicic systems remains an open one. On the one hand
378 the gradual nature of collapse at Bardarbunga and Fernandina contrasts with the highly punctuated
379 collapse style inferred during explosive silicic eruptions like Katmai and Pinatubo (*2*, *41*). In
380 addition, collapse at silicic volcanoes is generally considered to be triggered by eruption through a
381 central vent rather than through the lateral withdrawal mechanism seen at Bardarbunga. On the
382 other hand, of the two instrumentally monitored silicic collapses, the most silicic, Katmai was also
383 clearly associated with a lateral withdrawal. This mechanism could therefore be more widespread at
384 silicic calderas than commonly considered. In addition, the locations and mechanisms of the large,
385 apparently collapse-related earthquakes interpreted to denote punctuated collapses of Katmai and
386 Pinatubo are poorly constrained, such that a regional tectonic origin for them cannot be precluded
387 (*15*, *35*, *42*, *43*). Consequently, Bardarbunga 2014-15 provides our clearest picture yet of how
388 caldera collapse can be triggered during large eruptions, and how the dynamics of the subterranean
389 magma flow path and the interaction with magma reservoir pressure regulates eruption rates and the
390 rate of collapse.

391 **Acknowledgements**

392 A large part of the field effort was supported with crisis response funding from the Icelandic Government
393 through the Civil Protection Department of the National Commissioner of the Icelandic Police. A
394 considerable part of this work was made possible through the European Community‘s Seventh Framework
395 Programme Grant No. 308377 (Project FUTUREVOLC). Further support came from the EU Seventh
396 Framework Marie Curie project NEMOH No. 289976, and the project CO2Volc ERC grant No. 279802, the
397 Research Fund of the University of Iceland, the Irish Research Council, the Helmholtz Alliance on Remote
398 Sensing and Earth System Dynamics (EDA) and UNAM/CIC Intercambio Académico. We thank the

following key persons for help with instrumentation and data: B.H. Bergsson, V.S. Kjartansson, S. Steinthorsson, Th. Jónsson, P. Erlendsson, J. Soring, I. Jónsdóttir, G. Sverrisdóttir and G. Sigurdsson, the SIL network monitoring team at the IMO, the field observation team of the IES in Holuhraun, and for collaboration on seismic instruments and data we thank R.S. White and the Cambridge team and C. Bean and the UCD team. The subsidence of Bárðarbunga was mapped by the surveying aircraft of Isavia (Icelandic Aviation Operation Services) and from satellite images acquired by Pléiades (© CNES 2014, Distributed Airbus DS, subsidized access provided by the French Space Agency CNES's ISIS programme) and SPOT 6 (©Airbus DS 2014). Committee on Earth Observation Satellites (CEOS) and Geohazards Supersites and Natural Laboratories (GSNL) also provided access to satellite data. CSK data were provided by the Italian Space Agency (ASI) through the Iceland Volcanoes Supersite agreement. The Icelandic Coast Guard provided valuable aeroplane and helicopter support for the field effort. Field operations at Bárdarbunga were supported by the Landsvirkjun power company, the Iceland Glaciological Society and Vatnajökull National Park.

References

1. M. Branney, V. Acocella, "Calderas" in *The Encyclopedia of Volcanoes,* H. Sigurdsson, B. Houghton, H. Rymer, Eds. (Academic Press, Academic Press, Heidelberg, Amsterdam, Boston, ed. 2, 2015), pp. 229-315.

2. J. Stix, T. Kobayashi, Magma dynamics and collapse mechanisms during four historic caldera-forming events. *J. Geophys. Res.* **113**, JB005073 (2008).

3. A. R. McBirney, A historical note on the origin of calderas. *J. Volcanol. Geotherm. Res.* **42**, 303-306 (1990).

4. R. S. J. Sparks, P.W. Francis, R. D. Hamer, R. J. Pankhurst, L. O. O'callaghan, R. S. Thorpe, R. Page, Ignimbrites of the Cerro Galán caldera, NW Argentina. *J. Volcanol. Geotherm. Res.* **24**, 205-248 (1985).

5. T. H. Druitt, R. S. J. Sparks, On the formation of calderas during ignimbrite eruptions. *Nature* **310**, 679-681 (1984).

6. P. W. Lipman, Subsidence of ash-flow calderas: relation to caldera size and magma-chamber geometry. *Bull. Volc.*, **59**, 198-218 (1997).

7. V. Acocella, Understanding caldera structure and develpoment: an overview of analogue models compared to natural calderas. *Earth Sci. Rev.*, **125**, 125-160 (2007).

8. O. Roche, T. H. Druitt, O. Merle, Experimental study of caldera formation. *J. Geophys. Res.* **105**, 395-416 (2001).

9. T. Simkin, K. A. Howard, Caldera collapse in the Galapagos Islands, 1968: The largest known collapse since 1912 followed a flank eruption and explosive volcanism within the caldera. *Science* **169**, 429–437 (1970).

10. S. A. Fedotov, Y. K. Markhinin, *The Great Tolbachik Fissure Eruption. Geological and Geophysical Data 1975-1976.* (Cambridge University Press, Cambridge, 2011).

11. N. Geshi, T. Shimano, S. Chiba, Caldera collapse during the 2000 eruption of Miyakejima Volcano, Japan. *Bull. Volcanol*. **64**, 55-68 (2002).

12. T. Staudacher, V. Ferrazzini, A. Peltier, P. Kowalski, P. Boissier, P. Catherine, F. Lauret, F. Massin, The April 2007 eruption and the Dolomieu crater collapse, two major events at Piton de la Fournaise (La Réunion Island, Indian Ocean). *J. Volcanol. Geotherm. Res*. **184**, 126-137 (2009).

13. E. P. Holohan, M. P. J. Schöpfer, J. J. Walsh, J. J. Stress evolution during caldera collapse. Earth Planet. Sc. Lett. **421**, 139-151 (2015).

14. K. V. Cashman, G. Giordano, Calderas and magma reservoirs. *J. Volcanol. Geotherm. Res*. **288**, 28-45 (2014).

15. J. Battaglia, C. H. Thurber, J.-L. Got, C. A. Rowe, R A. White, Precise relocation of earthquakes following the 15 June 1991 eruption of Mount Pinatubo (Philippines). *J. Geophys. Res*. **109**, B7 (2004).

16. L. Michon, F. Massin, V. Famin, V. Ferrazzini, G. Roult, Basaltic calderas: Collapse dynamics, edifice deformation, and variations of magma withdrawal. *J. Geophys. Res*. **116**, B3 (2011).

17. H. Björnsson, P. Einarsson, Volcanoes beneath Vatnajökull, Iceland: evidence from radio-echo sounding, earthquakes and jökulhlaups. *Jokull* **40**, 147-148 (1990).

18. M. T. Gudmundsson, T. Högnadóttir, Volcanic systems and calderas in the Vatnajökull region, central Iceland, constraints on crustal structure from gravity data. Journal of Geodynamics, 43, 153-169 (2007).

19. T. Thordarson, G. Larsen, Volcanism in Iceland in historical time: Volcano types, eruption styles and eruption history. *J. Geodyn*. **43**, 118-152 (2007).

20. F. Sigmundsson, A. Hooper, S. Hreinsdóttir, K. S. Vogfjörd, B. G. Ófeigsson, E. R. Heimisson, S. Dumont, M. Parks, K. Spaans, G. B. Gudmundsson, V. Drouin, T. Árnadóttir, K. Jónsdóttir, M. T. Gudmundsson, T. Högnadóttir, H. M. Fridriksdóttir, M. Hensch, P. Einarsson, E. Magnússon, S. Samsonov, B. Brandsdóttir, R. S. White, T. Ágústsdóttir, T. Greenfield, R. G. Green, A. R. Hjartardóttir, R. Pedersen, R. A. Bennett, H. Geirsson, P. C. La Femina, H. Björnsson, F. Pálsson, E. Sturkell, C. J. Bean, M. Möllhoff, A. K. Braiden, E. P. S. Eibl, Segmented lateral dyke growth in a rifting event at Bárðarbunga volcanic system. *Nature* **517**, 191-195 (2015).

21. T. Ágústsdóttir, J. Woods, T. Greenfield, R. G. Green, R. S. White, T. Winder, B. Brandsdóttir, S. Steinthórsson, H. Soosalu, Strike-slip faulting during the 2014 Bárðarbunga-Holuhraun dike intrusion, central Iceland. *Geophys. Res. Lett*. (accepted). DOI: 10.1002/2015GL067423

22. S. R. Gíslason, G. Stefánsdóttir, M. A. Pfeffer, S. Barsotti, Th. Jóhannsson, I. Galeczka, E. Bali, O. Sigmarsson, A. Stefánsson, N. S. Keller, A. Sigurdsson, B. Bergsson, B. Galle, V. C. Jacobo, S. Arellano, A. Aiuppa, E. S. Eiríksdóttir, S. Jakobsson, G. H. Gudfinnsson, S. A. Halldórsson, H. Gunnarsson, B. Haddadi, I. Jónsdóttir, Th. Thordarson, M. Riishuus, Th. Högnadóttir, T. Dürig, G. B. M. Pedersen, A. Höskuldsson, M. T.

Gudmundsson, Environmental pressure from the 2014–15 eruption of Bárðarbunga volcano, Iceland. *Geochem. Perspect. Lett*., **1**, 84-93 (2015).

23. O. Roche, O., T. H. Druitt, Onset of caldera collapse during ignimbrite eruptions. Earth Planet. Sci. Lett., **191**(3), 191-202 (2001).

24. Materials and methods are available as supplementary materials on Science Online.

25. J. Browning, A. Gudmundsson, Surface displacements resulting from magma-chamber roof subsidence, with application to the 2014-2015 Bardarbunga-Holuhraun volcanotectonic episode in Iceland. *J. Volcanol. Geotherm. Res*. **308**, 82-98 (2015).

26. H. Björnsson, Hydrology of ice caps in volcanic regions. Soc. Sci. Isl. 45, 139pp (1988).

27. E. P. Holohan, V. R. Troll, B. Van Wyk de Vries, J. J. Walsh, T. R. Walter, Unzipping Long Valley: an explanation for vent migration during an elliptical ring fracture eruption. *Geology* **36**, 323-326 (2008).

28. E. P. Holohan, T. R. Walter, M.P. Schöpfer, J. J. Walsh, B. Wyk de Vries, V. R. Troll, Origins of oblique-slip faulting during caldera subsidence. J. Geophys. Res. **118**(4), 1778-1794 (2013).

29. C. Clough, H. Maufe, E. Baley, The cauldron subsidence of Glen-Coe, and the associated igneous phenomena. Q.J.Soc. Lond. **65**, 611–678 (1909).

30. H. Bathke, M. Nikhoo, E.P. Holohan, T.R. Walter, Insights into the 3D architecture of an active caldera ring-fault at Tendürek volcano through modeling of geodetic data. Earth. Planet. Sci. Lett. **422**:157-168 (2015).

31. A. Fichtner, H. Tkalcic, Insights into the kinematics of a volcanic caldera drop: Probabilistic finite-source inversion of the 1996 Bardarbunga, Iceland, earthquake. *Earth Planet. Sc. Lett*. **297**, 607-615 (2010).

32. B. Riel, P. Milillo, M. Simons, P. Lundgren, H. Kanamori, H., S. Samsonov, The collapse of Bárðarbunga Caldera, Iceland. *Geophys. J. Int*. **202**, 446-453 (2015).

33. S. Cesca, A. T. Sen, T. Dahm, Seismicity monitoring by cluster analysis of moment tensors. *Geophys. J. Int*. **196**, 1813-1826 (2013).

34. A. Shuler, G. Ekström, M. Nettles, Physical mechanisms for vertical-CLVD earthquakes at active volcanoes. J. Geophys. Res. **118**(4), 1569-1586 (2013).

35. K. Abe, Seismicity of the caldera-making eruption of Mount Katmai, Alaska in 1912. *B. Seismol. Soc. Am*. **82**, 175-191 (1992).

36. C. P. Montagna, H. M. Gonnermann, Magma flow between summit and Pu`u `O`o at Kilauea Volcano, Hawaii. *Geochem. Geophy. Geosy.* **14**, 2232–2246 (2013).

37. H. Kumagai, T. Ohminato, M. Nakano, M. Ooi, A. Kubo, H. Inoue, J. Oikawa, Very-long-period seismic signals and caldera formation at Miyake Island, Japan. Sci. 293, 687-690 (2001).

38. G. Wadge, Steady state volcanism: evidence from eruption histories of polygenetic volcanoes. J. Geophys. Res. **87**, B5: 4035-4049 (1982).

39. A. Geyer, A. Folch, J. Martí, Relationship between caldera collapse and magma chamber withdrawal: an experimental approach. J Volcanol. Geotherm. Res. **157**, 375-386 (2006).

40. A. Folch, J. Marti, Time-dependent chamber and vent conditions during explosive caldera-forming eruptions. *Earth Planet. Sc. Lett.* **280**, 246-253 (2009).

41. W. Hildreth, J. Fierstein, Katmai volcanic cluster and the great eruption of 1912. *Geophys. J. Int*. **112**, 446-453 (2000).

42. B. C. Bautista, M. L. P. Bautista, R. S. Stein, E. S. Barcelona, R. S. Punongbayan, E. P. Laguerta, A. R. Rasdas, G. Ambubuyog, E. Q. Amin, "Relationship of regional and local structures to Mount Pinatubo activity" in *Fire and Mud: Eruptions and Lahars of Mount Pinatubo, Philippines. PHIVOLCS*, C. G. Newhall, R. S. Punongbayan, Eds. (University of Washington Press, Quezon City, 1996), pp. 351-370.

43. J. Mori, R. A. White, D. H. Harlow, P. Okubo, J. A. Power, R. P. Hoblitt, E. P. Laguerta, A. Lanuza, B. C. Bautista, "Volcanic earth quakes following the 1991 climactic eruption of Mount Pinatubo: strong seismicity during a waning eruption" in *Fire and Mud: Eruptions and Lahars of Mount Pinatubo, Philippines. PHIVOLCS*. C. G. Newhall, R. S. Punongbayan, Eds. (University of Washington Press, Quezon City, 1996), pp. 339-350.

44. L. Michon, T. Staudacher, V. Ferrazzini, P. Bachèlery, J. Marti, April 2007 collapse of Piton de la Fournaise: a new example of caldera formation. *Geophys. Res. Lett*., **34**(21) (2007).

45. F. R. Fontaine, G. Roult, L. Michon, G. Barruol, A. Di Muro, The 2007 eruptions and caldera collapse of the Piton de la Fournaise volcano (La Reunion Island) from tilt analysis at a single very broadband seismic station. *Geophys. Res. Lett*. **41**, 2803-2811 (2014); published online EpubApr 28 (10.1002/2014GL059691).

46. A. Di Muro, N. Metrich, D. Vergani, M. Rosi, P. Armienti, T. Fougeroux, E. Deloule, I. Arienzo, L. Civetta, The Shallow Plumbing System of Piton de la Fournaise Volcano (La R,union Island, Indian Ocean) Revealed by the Major 2007 Caldera-Forming Eruption. *J. Petrol*. **55**, 1287-1315 (2014); published online EpubJul (10.1093/petrology/egu025).

47. T. Kaneko, A. Yasuda, T. Shimano, S. Nakada, T. Fujii, T. Kanazawa, A. Nishizawa, Y. Matsumoto, Submarine flank eruption preceding caldera subsidence during the 2000 eruption of Miyakejima Volcano, Japan. *Bull. Volcanol*. **67**, 243-253 (2005); published online EpubMar (10.1007/s00445-004-0407-1).

48. M. Amma-Miyasaka, M. Nakagawa, S. Nakada, Magma plumbing system of the 2000 eruption of Miyakejima Volcano, Japan. *Bull. Volcanol*. **67**, 254-267 (2005); published online EpubMar (10.1007/s00445-004-0408-0).

49. T. Nishimura, S. Ozawa, M. Murakami, T. Sagiya, T. Tada, M. Kaidzu, M. Ukawa, Crustal Deformation caused by magma migration in the northern Izu Islands, Japan. *Geophys. Res. Lett*. **28**, 3745-3748 (2001); published online EpubOct 1 (Doi 10.1029/2001gl013051).

50. S. A. Fedotov, L. B. Slavina, S. L. Senyukov, M. S. Kuchay, Seismic processes and migration of magma during the Great Tolbachik Fissure Eruption of 1975-1976 and Tolbachik Fissure Eruption of 2012-2013, Kamchatka Peninsula. *Izv. Atmos. Ocean Phy*. **51**, 667-687 (2015); published online EpubDec (10.1134/S000143381507004x).

51. S. A. Fedotov, I. S. Utkin, L. I. Utkina, The Peripheral Magma Chamber of Ploskii Tolbachik, a Kamchatka Basaltic Volcano: Activity, Location and Depth, Dimensions, and their Changes Based on Magma Discharge Observations. *J. Volcanol. Seismol*. **5**, 369-385 (2011); published online EpubDec (10.1134/S0742046311060042).

52. P. Doubik, B. E. Hill, Magmatic and hydromagmatic conduit development during the 1975 Tolbachik Eruption, Kamchatka, with implications for hazards assessment at Yucca Mountain, NV. *J. Volcanol. Geotherm. Res*. **91**, 43-64 (1999); published online EpubJul (Doi 10.1016/S0377-0273(99)00052-9).

53. S.A. Fedotov, A. M. Chirkov, N.A. Gusev,G. N. Kovalev, Y. B. Slezin, The large fissure eruption in the region of Plosky Tolbachik volcano in Kamchatka, 1975–1976. *Bull. Volcanol*. **43,** 47-60 (1980).

54. J. Filson, T. Simkin, L. K. Leu, Seismicity of a caldera collapse: Galapagos Islands 1968. J. Geophys. Res., **78**(35), 8591-8622 (1973).

55. J. E. Hammer, M. J. Rutherford, W. Hildreth, Magma storage prior to the 1912 eruption at Novarupta, Alaska. *Contrib. Mineral. Petr*. **144**, 144-162 (2002); published online EpubNov (10.1007/s00410-002-0393-2).

56. M. J. Rutherford, J. D. Devine, in *Fire and Mud: Eruptions and Lahars of Mount Pinatubo, Philippines* C. G. Newhall, R. S. Punongbayan, Eds. (Philippine Institute of Volcanology and Seismology & University of Washington Press, Quezon City, Seattle & London, 1996), pp. 751–766.

57. H. Kanamori, J. Mori, E. Hauksson, T. H. Heaton, L. K. Hutton, L. M. Jones, Determination of earthquake energy release and ML using TERRAscope. Bull. . Seismol. Soc. Am., **83**(2), 330-346 (1993).

58. M. Kikuchi, Y. Yamanaka, K. Koketsu, Source Process of the Long-period Seismic Pulses Associated with the 2000 Eruption of Miyakejima Volcano and its Implications. J. Geograph. Tokyo **110**(2), 204-216 (2001).

59. M. T. Gudmundsson, T. Hognadottir, A. B. Kristinsson, S. Gudbjornsson, Geothermal activity in the subglacial Katla caldera, Iceland 1999-2005, studied with radar altimetry. *Ann. Glacio*. **45**, 66-72 (2007).

60. C. Mätzler, Microwave permittivity of dry snow. *IEEE Trans. Geosci. Remote Sens*. **34**, 573-581 (1996).

61. C. Rossi, C. Minet, T. Fritz, M. Eineder, R. Bamler, Temporal monitoring of subglacial volcanoes with TanDEM-X—Application to the 2014–2015 eruption within the Bárðarbunga volcanic system, Iceland. Remote Sens. Environ. 181, 186-197 (2016)

62. T. Johannesson, H. Björnsson, E. Magnússon, S. Guðmundsson, F. Pálsson, O. Sigurðsson, T. Thorsteinsson, E. Berthier, Ice-volume changes, bias estimation of mass-balance measurements and changes in subglacial lakes derived by lidar mapping of the surface of Icelandic glaciers. *Ann. Glacio.* **54**, 63-74 (2013).

63. E. Magnusson, F. Palsson, H. Bjornsson, S. Gudmundsson, Removing the ice cap of Oraefajokull central volcano, SE-Iceland: Mapping and interpretation of bedrock topography, ice volumes, subglacial troughs and implications for hazards assessments. *Jokull* **62**, 131-150 (2012).

64. H. Bjornsson, F. Pálsson, M. T. Gudmundsson, *Vatnajokull, Northwest Part, 1:100 000: Bedrock topography*, Landsvirkjun and Science Institute, University of Iceland, 1992.

65. A. H. Jarosch, Icetools: A full Stokes finite element model for glaciers. *Comput. Geosci*. **34**, 1004-1014 (2008).

66. J. W. Glen, The Creep of Polycrystalline Ice. *P. Roy. Soc. A-Math. Phy*. **228**, 519-538 (1955).

67. K. M. Cuffey, W. S. B. Paterson, *The Physics of Glaciers.* (Elsevier Butterworth-Heinemann, Burlington, ed. 4, 2010).

68. C. E. Lesher, F. J. Spera, "Thermodynamic and Transport Properties of Silicate Melts and Magma" in *The Encyclopedia of Volcanoes*, H. Sigurdsson, B. Houghton, H. Rymer, Eds. (Academic Press, Academic Press, Heidelberg, Amsterdam, Boston, ed. 2, 2015), pp. 113-141.

69. R. Bödvarsson, S. T. Rögnvaldsson, R. Slunga, E. Kjartansson, The SIL data acquisition system—at present and beyond year 2000. *Phys. Earth Planet. Inter*. **113**, 89-101 (1999).

70. R. Slunga, S. T. Rögnvaldsson, R. Bödvarsson, Absolute and relative locations of similar events with application to microearthquakes in southern Iceland. *Geophys. J. Int*. **123**, 409–419 (1995).

71. S. Th. Rögnvaldsson, R. Slunga, Routine fault plane solutions for local networks: a test with synthetic data. Bull. Seism. Soc. Am. **83**.4, 1232-1247 (1993).

72. R. Stefánsson, R. Böðvarsson, R. Slunga, P. Einarsson, S. Jakobsdóttir, H. Bungum, S. Gregersen, J. Havskov, J. Hjelme, H. Korhonen, Earthquake prediction research in the South Iceland seismic zone and the SIL project. *Bull. Seism. Soc. Am*. **83**, 696–716 (1993).

73. S., A., R. Cesca, T. Dahm, Discrimination of induced seismicity by full moment tensor inversion and decomposition. *J. Seimsol*. **17**, 147-163 (2013).

74. P. A. Rosen, S. Hensley, I. R. Joughin, F. K. Li, S. N. Madsen, E. Rodriguez, R. M. Goldstein, Synthetic aperture radar interferometry, presented at *Proceedings of the IEEE,* 2000 (unpublished).

75. B. Kampes, Delft Object-oriented Radar Interferometric Software: User's Manual and Technical Documentation v4.02, presented at *Delft Technical University*, 1999 (unpublished).

76. Y. Y. Kagan, 3-D rotation of double-couple earthquake sources. *Geophys. J. Int*. **106**, 709–716 (1991).

77. R. M. Goldstein, C. L. Werner, Radar interferogram filtering for geophysical applications. *Geophys. Res. Lett*. **25**, 4035-4038 (1998).

78. C. W. Chen, H. A. Zebker, Two-dimensional phase unwrapping with use of statistical models for cost functions in nonlinear optimization. *J. Opt. Soc. Am. A Opt. Image. Sci. Vis.* **18**, 338-351 (2001).

79. Y. Okada, Internal deformation due to shear and tensile faults in a half-space. *B. Seismol. Soc. Am*. **82**, 1018-1040 (1992).

80. A. Hooper, J. Pietrzak, W. Simons, H. Cui, R. Riva, M. Naeije, A. Terwisscha van Scheltinga, E. Schrama, G. Stelling, A. Socquet, Importance of horizontal seafloor motion on tsunami height for the 2011 Mw=9.0 Tohoku-Oki earthquake. *Earth Planet. Sc. Lett*. **361**, 469-479 (2013).

81. C. E. Ford, D. G. Russell, J. A. Craven, M. R. Fisk, Olivine-liquid equilibria: Temperature, pressure and composition dependence of the crystal/liquid cation partition coefficients for Mg, Fe2+, Ca and Mn. *J. Petrol.* **24**, 256-266 (1983).

82. H. J. Yang, R. J. Kinzler, T. L. Grove, Experiments and models of anhydrous, basaltic olivine-plagioclase-augite saturated melts from 0.001 to 10 kbar. *Contrib. Mineral. Petr*. **124**, 1-18 (1996).

611 83. G. H. Gudfinnsson, D. C. Presnall, A pressure-independent geothermometer for primitive mantle melts.
612 *J. Geophys. Res*. **106**, B8 (2001).

613 84. K. D. Putirka, Thermometers and barometers for volcanic systems. *Rev. Mineral. Geochem*. **69**, 61-120
614 (2008).

615 85. Y. Kawakami, J. Yamamoto, H. Kagi, Microraman densimeter for CO2 inclusions in mantle derived
616 minerals. *Appl. Spectrosc*. **57**, 1333-1339 (2003).

617 86. M.R. Burton, P. Allard, F. Mure, A. La Spina, Magmatic gas composition reveals the
618 source depth of slug-driven Strombolian explosive activity, *Science*, **317**, 5835, 227-230 (2007),
619 doi:10.1126/science.1141900.
620
621 87. A. Aiuppa, C. Federico, G. Giudice, S. Gurrieri, Chemical mapping of a fumarolic field: La Fossa Crater,
622 Vulcano Island (Aeolian Islands, Italy), *Geophys. Res. Lett.*, **32** (13) (2005), p. L13309
623 http://dx.doi.org/10.1029/2005GL023207

624 88. P.-J. Gauthier, O. Sigmarsson, M. Gouhier, B. Haddadi, and S. Moune, Elevated gas flux and trace metal
625 degassing from the 2014–2015 fissure eruption at the Bárðarbunga volcanic system, Iceland, *J. Geophys.*
626 *Res. Solid Earth,* **121**, (2016) doi:10.1002/2015JB012111.

627 89. E. Bali, O. Sigmarsson, S. Jakobsson, H. Gunnarsson, Volatile budget of the Nornahraun eruption in the
628 Bárðarbunga system, Iceland. Geophysical Research Abstracts Vol. 17, EGU2015-5757, 2015 EGU General
629 Assembly (2015). http://meetingorganizer.copernicus.org/EGU2015/EGU2015-5757.pdf

630 90. A. Burgisser, M. Alletti, B. Scaillet, Simulating the behavior of volatiles belonging to the C–O–H–S
631 system in silicate melts under magmatic conditions with the software D-Compress, *Comput. Geosci.*, **79**, 1–
632 14.

633 91. D. O. Potyondy, P. A. Cundall, A bonded particle model for rock. *Int. J. Rock Mech. Min.* **41**, 1329-1364
634 (2004).

635 92. D. Mas Ivars, M. E. Pierce, C. Darcel, J. Reyes-Montes, D. O. Potyondy, R. P. Young, P. A. Cundall, The
636 synthetic rock mass approach for jointed rock mass modelling. *Int. J. Rock Mech. Min*. **48**, 219-244 (2011).

637 93. Itasca Consulting Group, Inc. *PFC2D - Particle Flow Code in Two-Dimensions, Ver. 5.0.* Minneapolis,
638 Itasca (2014).

639 94. K. Mogi, Relations between the eruptions of various volcanoes and the deformations of the ground
640 surfaces around them. *B. Earthq. Res. Inst. Univ. Tokyo* **36**, 99–134 (1958).

641 95. M. Ripepe, D. Delle Donne, R. Genco, G. Maggio, M. Pistolesi, E. Marchetti, G. Lacanna, G. U. P. Poggi,
642 Volcano seismicity and ground deformation unveil the gravity-driven magma discharge dynamics of a
643 volcanic eruption. *Nat. Commun*. **6** (2015).

644 96. Y. Bottinga, D. Weill, The viscosity of magmatic silicate liquids: a model for calculation. *Am. J. Sci*. **272**,
645 438–475 (1972).

646

One page summary:

Gradual caldera collapse at Bárdarbunga volcano, Iceland, regulated by lateral magma outflow

Magnús T. Gudmundsson[1], Kristín Jónsdóttir[2], Andrew Hooper[3], Eoghan P. Holohan[4,5], Saemundur A. Halldórsson[1], Benedikt G. Ófeigsson[2], Simone Cesca[4], Kristín S. Vogfjörd[2], Freysteinn Sigmundsson[1], Thórdís Högnadóttir[1], Páll Einarsson[1], Olgeir Sigmarsson[1,6], Alexander H. Jarosch[1], Kristján Jónasson[7], Eyjólfur Magnússon[1], Sigrún Hreinsdóttir[8], Marco Bagnardi[3], Michelle M. Parks[1], Vala Hjörleifsdóttir[9], Finnur Pálsson[1], Thomas R. Walter[4], Martin P.J. Schöpfer[10], Sebastian Heimann[4], Hannah I. Reynolds[1], Stéphanie Dumont[1], Eniko Bali[1], Gudmundur H. Gudfinnsson[1], Torsten Dahm[4], Matthew Roberts[2], Martin Hensch[2], Joaquín, M.C. Belart[1], Karsten Spaans[3], Sigurdur Jakobsson[1], Gunnar B. Gudmundsson[2], Hildur M. Fridriksdóttir[1,2], Vincent Drouin[1], Tobias Dürig[1], Gudfinna Adalgeirsdóttir[1], Morten S. Riishuus[1], Gro B.M. Pedersen[1], Tayo van Boeckel[1] , Björn Oddsson[11], Melissa A. Pfeffer[2], Sara Barsotti[2], Baldur Bergsson[2], Amy Donovan[12], Mike R. Burton[13], Alessandro Aiuppa[14]

INTRODUCTION: The Bárdarbunga caldera volcano in central Iceland collapsed from August 2014 – February 2015 during the largest eruption in Europe since 1784. An ice-filled subsidence bowl 8 x11 km wide and up to 65 m deep developed, while magma drained laterally for 45 km along a subterranean path and erupted as a major lava flow northeast of the volcano. Our data provide unprecedented insight into of the workings of a collapsing caldera.

RATIONALE: Collapses of caldera volcanoes are, fortunately, not very frequent, as they are often associated with very large volcanic eruptions. On the other hand, the rarity of caldera collapses limits insight into this major geological hazard. Since the formation of Katmai caldera in 1912, during the 20th century's largest eruption, only five caldera collapses are known to have occurred

before that at Bárdarbunga. We used aircraft-based altimetry, satellite photogrammetry, radar interferometry, ground-based GPS, evolution of seismicity, radio-echo soundings of ice thickness, ice flow modeling and geobarometry to describe and analyze the evolving subsidence geometry, its underlying cause, the amount of magma erupted, the geometry of the subsurface caldera ring faults and the moment tensor solutions of the collapse-related earthquakes.

RESULTS: After initial lateral withdrawal of magma for some days though a magma-filled fracture propagating through the Earth's upper crust, pre-existing ring faults under the volcano were reactivated over the period 20-24 August, marking the onset of collapse. On August 31, the eruption started and it terminated when the collapse stopped, having produced 1.5 km^3 of basaltic lava. The subsidence of the caldera declined with time in a near exponential manner, in phase with the lava flow rate.

The volume of the subsidence bowl was about 1.8 km^3. Using radio-echo soundings, we find that the subglacial bedrock surface after the collapse is down-sagged with no indications of steep fault escarpments. Using geobarometry, we determined the source depth of the magma to be approximately 12 km and modelling of geodetic observations gives a similar result. High precision earthquake locations and moment tensor analysis of the remarkable magnitude M5 earthquake series are consistent with steeply dipping ring faults. Statistical analysis of seismicity reveals communication over tens of kilometers between the caldera and the dyke.

CONCLUSIONS: We conclude that interaction between the pressure exerted by the subsiding reservoir roof and the physical properties of the subsurface flow path explain the gradual near exponential decline of both collapse rate and the intensity of the 181-day long eruption. By combining our various data sets, we show that the onset of collapse was caused by outflow of magma from underneath the caldera when 12-20% of the total magma intruded and erupted had flowed from the magma reservoir. However, the continued subsidence was driven by a feedback between the pressure of the piston-like block overlying the reservoir, and the 47 km long magma

outflow path. Our data provide better constraints on caldera mechanisms than previously available, demonstrating what caused the onset, and how both the roof overburden and the flow path properties regulate the collapse.

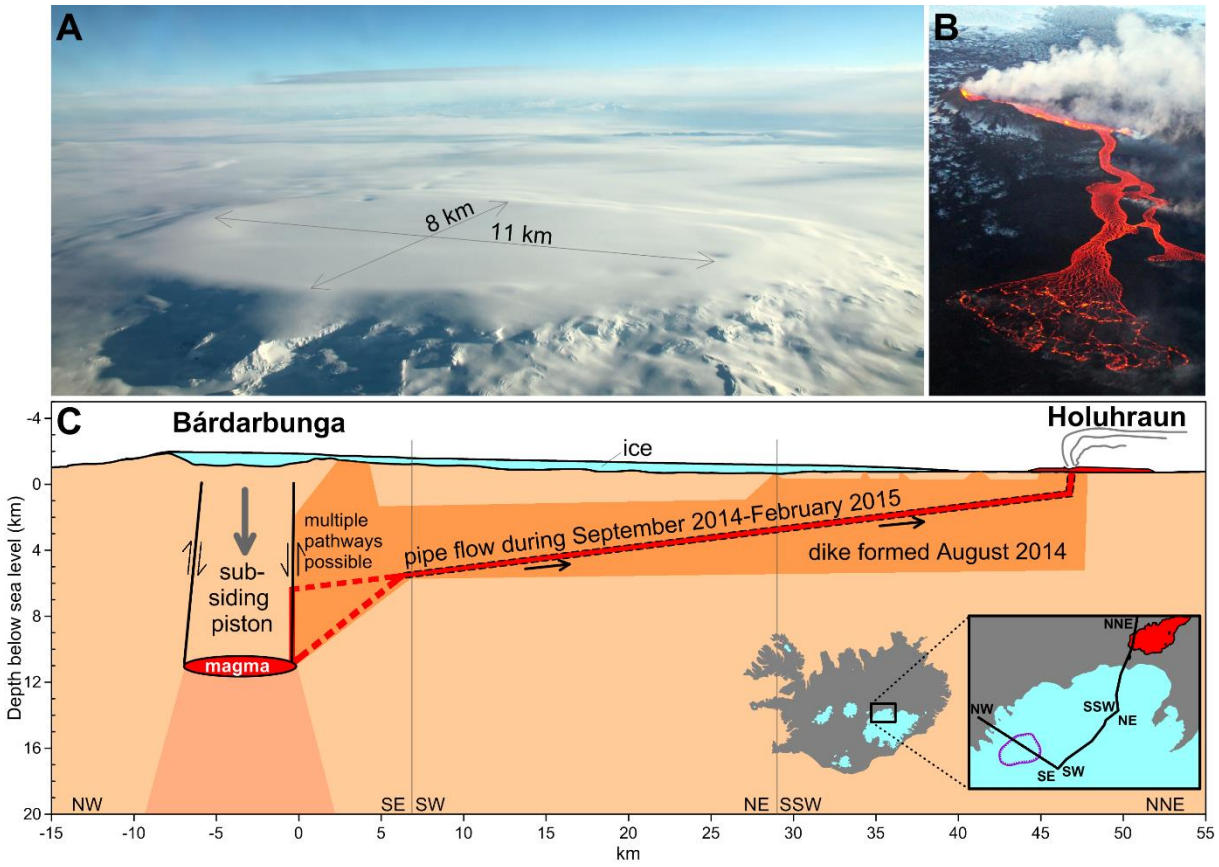

The Bárdarbunga caldera and the lateral magma flowpath to the Holuhraun eruption site. (**A**) Aerial view of the ice-filled Bárdarbunga caldera on 24 October 2014, view from the north. (**B**) The effusive eruption in Holuhraun, 45 km to the northeast of the caldera. (**C**) A schematic cross-section through the caldera and along the lateral subterranean flow path between the magma reservoir and the surface.

Supplementary Materials for

Gradual Caldera Collapse at Bárdarbunga Volcano, Iceland, Regulated by Lateral Magma Outflow

Magnús T. Gudmundsson,* Kristín Jónsdóttir, Andrew Hooper, Eoghan P. Holohan, Saemundur A. Halldórsson, Benedikt G. Ófeigsson, Simone Cesca, Kristín S. Vogfjörd, Freysteinn Sigmundsson, Thórdís Högnadóttir, Páll Einarsson, Olgeir Sigmarsson, Alexander H. Jarosch, Kristján Jónasson, Eyjólfur Magnússon, Sigrún Hreinsdóttir, Marco Bagnardi, Michelle M. Parks, Vala Hjörleifsdóttir, Finnur Pálsson, Thomas R. Walter, Martin P.J. Schöpfer, Sebastian Heimann, Hannah I. Reynolds, Stéphanie Dumont, Eniko Bali, Gudmundur H. Gudfinnsson, Torsten Dahm, Matthew Roberts, Martin Hensch, Joaquín, M.C. Belart, Karsten Spaans, Sigurdur Jakobsson, Gunnar B. Gudmundsson, Hildur M. Fridriksdóttir, Vincent Drouin, Tobias Dürig, Gudfinna Adalgeirsdóttir, Morten S. Riishuus, Gro B.M. Pedersen, Tayo van Boeckel, Björn Oddsson, Melissa A. Pfeffer, Sara Barsotti, Baldur Bergsson, Amy Donovan, Mike R. Burton, Alessandro Aiuppa

.

* correspondence to: mtg@hi.is

This PDF file includes:

Materials and Methods

Mapping of collapse

Ice surface topography was mapped 18 times in the period September 5, 2014 to June 4, 2015 (Fig. S1). An aircraft-based system (*59*) of sub-meter differential GPS and ground clearance altimeter (4.3 GHz wave, vertical elevation accuracy ±2 m) on board the survey aircraft of Isavia, the Icelandic Civil Aviation Service (*59*) provided 13 maps (Marked as FMS on Fig. S1). Survey lines were flown at 70-120 m ground clearance, measuring 4 times/sec. (at ~15 m intervals), and included coverage of the growing geothermal ice cauldrons. Comparison with kinematic GPS ground surveys in November, February and June (accuracy ±0.3 m), as well as snow temperature models and measurements show that the reflecting surface was unaffected by accumulation of winter snow and remained at the September 2014 summer surface until October, after which it gradually migrated downwards to ~1.5 m below it by February 2015. The reflecting surface probably indicates the lower boundary of the dry snow layer where snow temperature was <0°C (*60*). A subset of this data was used by Rossi et al. (*61*) to compare with Tandem-X derived maps of the subsidence for specific dates in late 2014. Optical photogrammetry maps were made using satellite data for August 28 (Spot 6 satellite), September 20 and October 10 (Pléiades satellite). Combined, the surface data provide a record of collapse volume with time (Fig. 3B). The curve in Fig. 3B is drawn using the difference of the running average of volume obtained in three adjacent surveys. The rate of volume change obtained in this way is also used in Fig. 6B. A continuously recording GPS station (BARC) was installed on the ice-surface on September 12, 2014. This station monitored the subsidence continuously for a large part of the unrest, although snow covering the antenna lead to some data gaps. A detailed ground kinematic GPS survey within and around the caldera on June 3-10, 2015 allowed the margins of collapse to be determined. Measurements of winter accumulation in the Bárdarbunga caldera in June 2015 constrained subsidence data while a glacier surface lidar map from 2011-2012 (*62*) was used as reference surface.

Radio-echo soundings (RES)

On February 3, 2015, when over 95% of the subsidence had occurred, 45 km of RES-profiles (1-5 MHz receiver bandwidth) were measured in over-snow traverses, covering about 2/3 of the caldera floor, including a large part of the subsided area. Bedrock echoes were detected for ~90% of the measurements. Along-profile bedrock echoes in length-depth coordinates were migrated (*63*) to compensate for the width of the radar beam (~200 m). Comparison of our data with previous mapping done in 1985 (*64*) indicates that the over 60 m subsidence had not caused significant changes in ice thickness; the maximum thickness observed is close to 800 meters on both occasions.

Ice flow modelling

Assuming no basal slip ($\mathbf{v}_b = 0$), ice deformation within the caldera has been computed using a Full-Stokes finite element model solving the standard equations (*65*). On the lateral boundaries of the model domain, no flow conditions (i.e. $\mathbf{v} = 0$) have been defined and the model domain chosen to be sufficiently large so that the lateral boundary conditions do not influence the ice flow within the caldera. The rate factor in Glen's flow law (*66*) has been estimated by constraining the horizontal model surface velocities to fit the measured ones at the BARC GPS station for the period September 12 to February 3. This yielded $A=1.6\ 10^{-24}$ $Pa^{-3}s^{-1}$ assuming the nonlinearity parameter in Glen's flow law to be n=3. This is somewhat stiffer than textbook values for temperate ice ($A=2.4\ 10^{-24}$ $Pa^{-3}s^{-1}$, ref. *67*) but is to be expected in a volcanic setting

where the ice body contains several tephra layers. Moreover, this low value for A supports our initial assumption of no basal slip. At the basal boundary, the post-collapse bed topography from the RES survey has been used and the surface of each model utilized the respective surface DTM implemented as a free surface within the FEM model. The ice flow modelling (Fig. S2) indicates that the ice surface subsidence was almost identical to bedrock subsidence everywhere in the caldera (error <1 m) in September-October. However, by the end of February the inflow of ice towards the bottom of the subsidence structure had resulted in uplift of about 3 m in the center and a subsidence of 1-3 m on a circle around the uplifted central part.

Lava volume and flow rate

The surface elevation of the growing Holuhraun lava flow was measured using a Theodolite from the ground in September 21 2014, and with the Isavia aircraft (see above on mapping of collapse) on November 4 and 26, December 4 and 30 and January 21, as well as later surveys in 2015. The aircraft surveys were calibrated with kinematic GPS profiling of the surface. These data give lava volumes at the time of survey, providing estimates of the average magma flow rate over periods of some weeks (Fig. 6B) and a final lava volume of 1.5±0.2 km^3. Nettleton gravity profiles obtained in September 2015 of the lava indicate average bulk lava density of 2500±100 kg m^{-3}. Using a basaltic magma density of 2750 kg m^{-3} for pressure of 300-400 MPa (*68*) the equivalent volume of magma at ~12 km depth in the crust is 1.4±0.2 km^3.

Relative locations of microearthquakes

M ≤2 earthquakes at the caldera recorded at distances <100 km between August 1 and October 17 by the Icelandic national seismic network, SIL (*69*) were relatively relocated using a standard 1D velocity model (*70*). SIL magnitudes were calculated according to Rognvaldsson and Slunga (*71*). A double-difference method was used, where absolute and relative arrival times of P and S waves determined through cross-correlation of waveforms, were inverted for best locations in multiple overlapping groups (*72*). Depth is set to zero at bedrock caldera floor (1.2 km above sea level, see Figs. 5 and 6). The relocated events roughly follow the north and south caldera rims; mostly being outside the northern rim and ~1 km inside the southern rim (Fig. 5A-B). Stability tests of relocations with subsets of events and stations indicated perturbations to event latitudes, particularly on the northern rim, probably due to slow velocities inside the caldera.

The InSAR detected subsidence associated with a M5.3 event on 18 September places the surface fault at ~2.5 km inside the pre-existing topographic northern caldera rim (Fig. S7), while the seismic epicentre location is just north of the northern caldera rim. Using the InSAR observation to locate the surface expression for the steeply outwards dipping caldera fault, the microearthquakes were shifted southward according to: *New lat = old lat * 0.883 +7.552.* The shifted locations are used in Figure 5. The shift is of the same order as the absolute error in the hypocentre locations. However, besides fitting the hypocentres to the InSAR-located fault it provides more consistency to S-P times from 82 events observed on an accelerometer at location BARC (Fig1A) from November 2014 to February 2015.

Moment tensor inversion and classification

The steady subsidence of the caldera was accompanied by a sequence of episodic M>5 earthquakes, which excited low frequency signals recorded at regional distances throughout Iceland. We performed a regional moment tensor inversion for all events with M>5, adopting a full moment tensor (MT) point source approximation, neglecting higher order moment tensor. The MT inversion (*73*) was performed by fitting full waveforms 3-component displacements at regional distances (40-200 km), in the low frequency band 0.01-0.05 Hz. We obtain centroid location, centroid depth and full MT solutions for 77 earthquakes at the caldera and with M > 5. MTs were decomposed into double couple (DC), compensated linear vector dipole (CLVD) and isotropic (ISO) components. Since MTs mostly differ in their DC components, we classified upon the similarity of the DC orientation using a clustering algorithm (*73*) and the normalized Kagan angle (*74*) as norm.

Waveform similarity analysis and moment estimation

To extend the interpretation of source processes to smaller events, where MT inversion becomes less stable, we apply a waveform similarity analysis. The scaling of the low frequency signals of weaker events and larger ones with similar waveforms is used to infer the scalar moment of smaller events (M < 5) from the known moment of the larger ones, resulting from the MT inversion procedure. In this way, we are able to estimate scalar moments for more than 600 events (352 with Mw > 4.0), down to a magnitude of Mw 3.3. These results allow tracking of the details of the temporal evolution of the moment release.

Mechanism corrected relative location

Moment tensor inversion provides a first estimate of centroid location and depth. A more precise location can be obtained by using relative location techniques, here also favored by the high waveform similarity. However, waveform-based lag-times can be affected by the dissimilarity among waveforms for the two families of events. To overcome this problem, we corrected cross-correlation lag times, by using corrections based upon focal mechanisms. The adopted procedure includes the computation of synthetic seismograms for different observed source mechanisms, the cross-correlation of synthetic waveforms to estimate fictitious time lags due to different focal mechanisms, and the inference of a time lag correction for each possible focal mechanism pair. As a result, we improved epicentral locations for 227 events. In order to obtain absolute locations, we combine the relative centroid locations of the largest events with the new absolute epicentral locations, imposing the condition that the mean centroid locations correspond to the mean absolute locations for both the northern and the southern cluster.

Caldera-dike seismicity correlations

The histogram shown in Figure 6A is computed using a simple model using the number of dyke earthquakes in 1.5 hour bins before and after (i) 4 < M < 4.6 and (ii) M > 4.6 caldera earthquakes (61). For example, the height of the fourth bar is found by assuming that the rate of dyke earthquakes during the 1.5 hours immediately preceding an $M \geq 4.6$ caldera earthquake is α times the reference rate, and estimating α with maximum likelihood, giving α=1.96. The plot can be read as, for example, the expected rate of dyke earthquakes is increased by 96% in the time interval 1.5 hours before an $M \geq 4.6$ caldera earthquake.

P-values are computed with a likelihood ratio test, and the confidence intervals are likelihood based. The reference rate (equal to 1 in Fig. 6A) is the rate of earthquake occurrence in periods more than three hours before or after caldera earthquakes of size M > 4. All dyke earthquakes that fall in one of the bins of Figure 6A together with all the dyke earthquakes in the reference periods are considered. The null hypothesis is that the portion of these earthquakes that fall in the bin is binomially distributed with parameter corresponding to a constant reference rate. To minimize the effect of the varying reference rate between months, the model assumes that this holds for each calendar month, and the final likelihood used in the test is the product of the likelihoods of individual months.

GPS analysis

The high-resolution GPS time series at BARC in the center of the caldera (Fig. 3C) was obtained using RTKLIB software, processing the receiver locations every 15 seconds as kinematic baselines from the HOFN reference station in southeast Iceland. Other GPS data were analyzed using the GAMIT/GLOBK software, version 10.6 using over 100 global reference stations to evaluate site positions in the ITRF08 reference frame. For the regional network average daily station positions were estimated. For the caldera GPS station (BARC) we furthermore divided the data into eight hour sessions using a 24 hour running window of reference station and orbit data. In the processing we solve for station coordinates, satellite orbit and earth rotation parameters, atmospheric zenith delay every two hours, and three atmospheric gradients per day. The IGS08 azimuth and elevation dependent absolute phase center offsets were applied to all antennas and ocean loading was corrected for using the FES2004 model.

InSAR analysis

We utilized X-band (wavelength 3.11 cm) radar images acquired by the COSMO-SkyMed constellation and employed two-pass Interferometric Synthetic Aperture Radar (InSAR) analysis (*75*) to measure ground deformation at Bárdarbunga caldera over 24-hr periods during which large caldera earthquakes occurred. The interferograms were processed using DORIS software (*76*) and a merged LiDAR, intermediate TanDEM-X, ASTER and EMISAR DEM was used to remove topographic fringes (*77*). To account for the large changes in topography over the caldera during the eruption, we interpolated the digital elevation model, using data from the continuous GPS station located inside the caldera. The wrapped interferometric phase values were filtered using an adaptive filter (*78*) and unwrapped with SNAPHU software (*79*). The one-day interferogram spanning September 17-18, 2014 was used to infer the location of faults that slipped during this period, which included a large caldera (M5.3) earthquake (Fig. S7). We modelled the fault system as a series of 30 rectangular vertical faults (*79*) with varying strike, and estimated location, size, minimum depth beneath the surface, and slip for each segment. Note, the data could be fitted equally well with steeply dipping faults, in either direction, but we fixed them to be vertical for convenience. The southern margin did not slip in this 24-hour interval and the model therefore does not constrain the actual location of the southern caldera fault. The contracting body at the base of the fault system was also modelled as a closing rectangular dislocation with uniform contraction (*79*). We used a Markov-chain Monte Carlo approach to estimate the multivariate probability distribution for all model parameters (*80*).

894 Petrological analysis and thermobarometry

895 Major element compositions of minerals and glasses were analyzed using a JEOL JXA-8230 electron
896 microprobe at the Institute of Earth Sciences, University of Iceland. Fluid inclusions within phenocrysts
897 were analysed by optical microscopy and confocal Raman spectroscopy (Horiba Jobin Yvon LabRAM HR800)
898 at the Bayerisches Geoinstitut, Bayreuth, Germany. Eruption temperatures calculated with different
899 thermometers (*81-83*) for the erupted lava are consistently in the range 1165-1180°C, in good agreement
900 with on-site measurements by thermal imaging cameras. Three independent thermobarometers were used
901 to constrain the depth of magma accumulation before the onset of the eruption; *(i) Glass thermobarometry*
902 was carried out using the fractional crystallization model of Yang et al. (*82*), which was calibrated using
903 basaltic melt compositions, *(ii) Clinopyroxene-Liquid Thermobarometry* was carried out based on the
904 clinopyroxene-liquid barometers published by Putirka (*84*) that rely on the pressure and temperature
905 dependence of Fe, Mg, Al and Na partitioning between pyroxenes and coexisting melt, and *(iii) CO_2 Density*
906 *Barometry* which is based on the principle that distance between the two Raman bands of CO_2 (in the
907 wavenumber region between 1250 and 1450 cm^{-1}) is a function of fluid density (*85*). In combination with
908 information on the temperature of the system, the entrapment pressure can be estimated based on the
909 equation of state of CO_2.

910

911 Subaerial gas composition analysis

912 The composition of the subaerial eruptive gases was measured by open-path Fourier Transform Infrared
913 spectrometer (FTIR) (*86*) on September 3, 19, 20 and 21 using the erupting lava as an infrared radiation
914 source, and Multi-Component Gas Analyzer System (MultiGAS) (*87*) on September 1, 21, October 8, January
915 26 and Feburary 6. The MultiGAS measurements were taken downwind from vent when the plume was
916 grounded. Major element composition and wt% of volatiles of the melt were defined using the average of
917 four clinopyroxene-hosted melt inclusions (*88*, *89*) and used as input to the D-COMPRESS magma/volatile
918 partition software (*90*). The model was run from atmospheric pressure to 600 MPa (18 km). The simulation
919 results indicate that the sulfur reaches 1600 ppm, the highest concentrations measured in melt inclusions
920 most representative of the pre-eruptive magma composition (*88*), at 470±100 MPa (14±3 km). This
921 estimate is partly dependent on the solubility constants provided for basalt. However, it convincingly
922 supports the petrological and geodetic estimates.

923

924 DEM modelling

925 We evaluated the role of pre-existing ring fault structures on the 2014-15 collapse by using the two-
926 dimensional Distinct Element Method (DEM) software PFC 5.0 (*90*). The DEM models comprise a 40 × 25 km
927 gravitationally-loaded assemblage of rigid circular particles that interact according to frictional-elastic
928 contact laws (*91*). Particles have a uniform size distribution, with radii between 60 m and 100 m, and a
929 density of 2700 kgm^{-3}. The model's basal and the lateral boundaries are frictionless rigid walls. Inter-particle
930 and particle-wall contacts have a Young's modulus of 70 GPa and a normal to shear stiffness ratio of 2.5.
931 The model comprises three regions (Fig. 5D): (i) A laccolith-like 'magma reservoir'. (ii) A fault-bound
932 reservoir 'roof'. (iii) The 'host rock' around the reservoir and roof. Within the reservoir, the contact friction
933 is 0.01 and particles are not bonded. Outside the reservoir, the contact friction coefficient is 0.5 and
934 particles are bonded with linear elastic beams. Bond tensile and shear strengths are 35 MPa in the roof and
935 70 MPa in the surrounding host rock. Note that fracturing of the weaker 'roof' zone will reduce the

assembly-scale strength and modulus here, locally by up to an order of magnitude (*27*), as suggested for Bardabunga by Riel et al. (*32*). Pre-existing faults, extending from the lateral edges of the reservoir to a few kilometres below the surface (Fig. 5D), are modelled by using a contact law for 'smooth' discontinuities in poly-disperse particle assemblages (*92*). The normal and shear stiffness of these 'fault' contacts is 60 GPa/m. Withdrawal of magma is assumed to occur laterally out of the 2D model plane (Fig. 5D) and is simulated by slowly reducing the areas of the reservoir particles. Displacements of surface particles were smoothed by a standard moving mean method to minimize localized particle effects. Our modelling comprised a series of forward simulations in which the dip of each fault was varied between 80-90 degrees, initial fault depths varied from 1-3 km, and chamber width varied from 7.0-8.5 km. Chamber depth was fixed at 12 km, based on the geobarometry data, to reduce the parameter space. The lateral position of the chamber was allowed to vary depending on the fault geometry, so that the faults lay within the clouds of hypocentres and projected upward to within the caldera. Effects of Young's modulus, strength and fault friction were also systematically tested. Further details on DEM modelling of caldera collapse are given in Holohan et al. (*27*, *93*).

Geodetic depth model

To determine the approximate depth of the magma chamber, we modelled post-rifting InSAR and GPS data (Fig. S3) using a point pressure source in an elastic halfspace (*94*). The depth range at 95% confidence is 8-12 km.

Coupled caldera subsidence and eruption model

We assume piston failure occurs approximately at a constant stress threshold, causing the pressure at the top of magma chamber to remain constant on average. Therefore, we ignore compressibility and assume that the density of the magma remains constant. The driving overpressure is then given by

$$\Delta P = \frac{W-F}{A} + \rho g h - \rho g d \qquad (1),$$

where *W* is the weight of the piston, *F* is the resistive force (friction), *A* is the cross sectional area of the magma chamber, *ρ* is the density of the magma, *g* is gravitational acceleration, h is the height of magma above the chamber exit point and *d* is the depth of the chamber exit point relative to the eruption site (Ext. Data 7). Conservation of mass implies

$$A\frac{dh}{dt} = -\pi r^2 v \qquad (2),$$

where *v* is the mean magma flow speed and r is conduit radius. Assuming that the time-averaged resistive force due to friction, *F,* and *d* remain constant, differentiating (1) and substituting (2) gives

$$\frac{d\Delta P}{dt} = -\rho g \frac{\pi r^2}{A} v \qquad (3).$$

Assuming pressure loss due to viscous drag from laminar flow in a cylindrical pipe (Hagen Poiseuille flow) and dynamic pressure loss on exit

$$\Delta P = \frac{8\eta L}{r^2} v + \frac{\rho}{2} v^2 \qquad (4)$$

$$\Longrightarrow v = -\frac{8\eta L}{\rho r^2} + \sqrt{\left(\frac{8\eta L}{\rho r^2}\right)^2 + 2\frac{\Delta P}{\rho}} \qquad (5).$$

We assume a cylindrical pipe, as models of thermal erosion predict that the cross section of a magma flow channel will evolve to be circular in shape, but note that for a non-circular cross section, the first term will still be proportional to the velocity, but with a different constant.

Expanding (5) gives

$$\Longrightarrow v = -\frac{8\eta L}{\rho r^2} + \frac{8\eta L}{\rho r^2} + \frac{r^2 \Delta P}{8\eta L} + O\left(\frac{r^2}{\eta L}\right)^2 = \frac{r^2 \Delta P}{8\eta L} + O\left(\frac{r^2}{\eta L}\right)^2 \qquad (6).$$

Substituting (6) into (3) gives

$$\frac{d\Delta P}{dt} = -\frac{\pi \rho g r^2}{A}\left[\frac{r^2 \Delta P}{8\eta L} + O\left(\frac{r^2}{\eta L}\right)^2\right] \qquad (7).$$

When $L >> r^2$, this reduces to

$$\frac{d\Delta P}{dt} = -\frac{\pi \rho g r^4}{8A\eta L}\Delta P \qquad (8)$$

$$\Longrightarrow \Delta P = \Delta P_0 e^{-\frac{\pi \rho g r^4}{8A\eta L} t} \qquad (9)$$

999 and

1000 $$h - h_\infty = (h_0 - h_\infty)e^{-\frac{\pi\rho g r^4}{8A\eta L}t}$$ (10).

1001

1002 A similar relationship has been derived to explain gravity-driven eruptions at Stromboli (*95*). Assuming that
1003 $h_0 - h_\infty$ is equal to the subsidence measured at the BARC GPS station, a best fit solution is $h_0 - h_\infty$ = 67.5 m
1004 and $\frac{\pi\rho g r^4}{8A\eta L}$ = 1.5 × 10^{-7} (Fig. 3B). A similar fit is obtained for magma flow rate and caldera volume change in
1005 Fig. 6B. Substituting ρ = 2700 kgm^{-3} (ref. *64*), g = 9.8 ms^{-2}, L = 47 km and ν=22 Pa s using the average glass
1006 compositions of the Holuhraun lava (*96*), gives ΔP_0 = 1.7 MPa and $\frac{r^4}{A}$ = 1.5 × 10^{-5} m^2. Constraining the
1007 eruption rate to be 250 m^3/s on 31 August, gives A= 32 km^2 and r = 4.7 m. This can be considered the
1008 effective radius of the flow path assuming circular cross sectional area. A similar relation would hold for
1009 other possible geometrical forms of the flow path cross sectional area. Theoretically, the eruption would
1010 approach equilibrium (ΔP=0 in (1)) asymptotically, but choking of the conduit due to cooling, slow-moving
1011 magma is expected before that.

1012

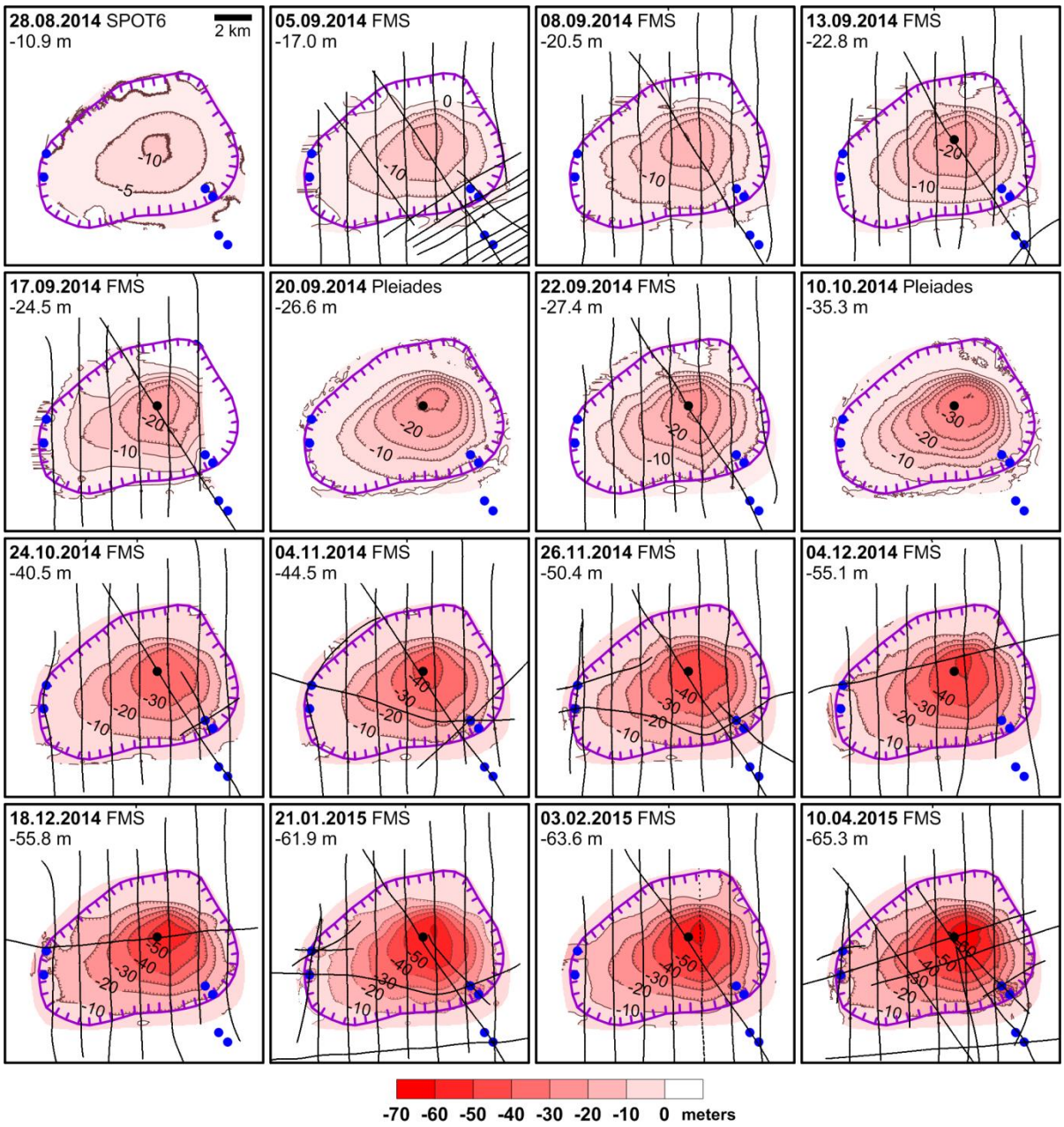

1013

1014 **Fig. S1.**

1015 **Maps of collapse** – margins as in Fig. 1C. The maps are corrected for ice flow (Fig. S2) and migration of
1016 reflector into the autumn 2014 surface due to propagation of cold wave into the firn in October-April (24).
1017 The number underneath the date gives the maximum subsidence. Three maps are obtained through
1018 satellite photogrammetry (28.08 – Spot 6, 20.09 and 10.10 from Pléiades) while the remaining 13 maps
1019 (marked as FMS) are obtained using an aircraft-combining radar altimetry and a submeter Differential GPS;
1020 the maps are made by interpolation between the profiles (shown as black lines)(24).

1021

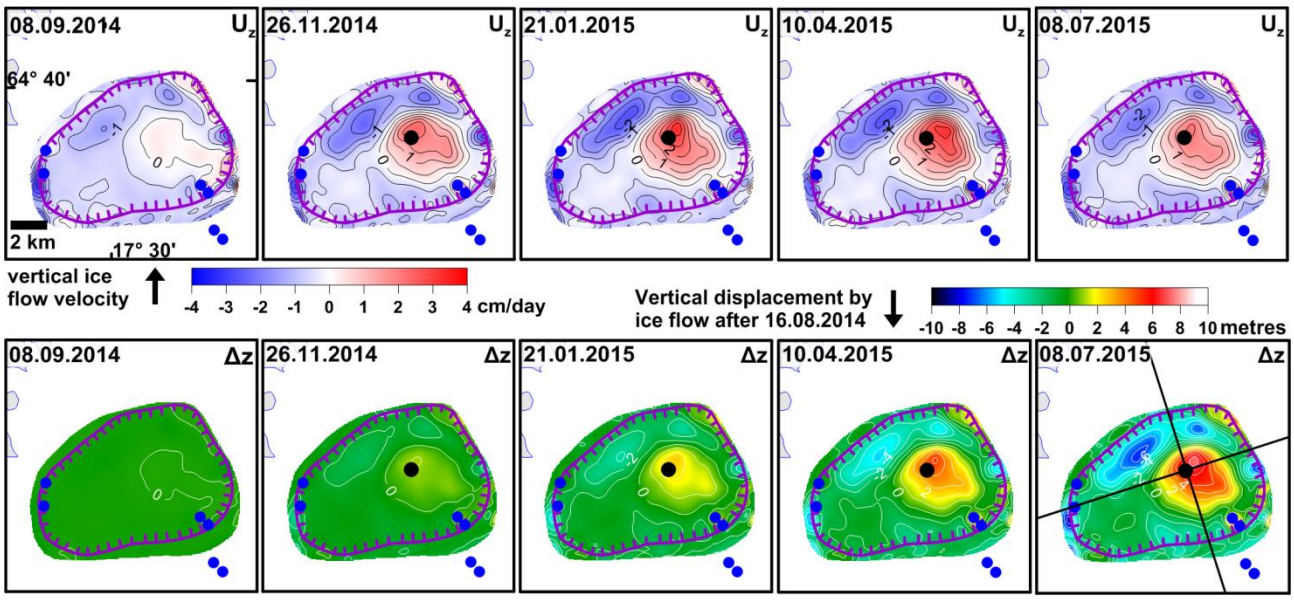

Fig. S2

Results of 3-D Full-Stokes ice flow models (see Materials and Methods) of the response of the glacier within the caldera to the subsidence for five dates spanning the period of collapse. The upper row shows vertical ice flow velocity while the lower row shows the accumulated surface elevation change due to the ice flow for the same dates. The model flow rates are constrained to fit the horizontal displacement of the GPS station BARC in the caldera center from September to February (see Materials and Methods). The maximum vertical ice flow velocity is modelled as having been about 3 cm per day on April 10, 2015. The accumulated uplift for end of eruption on February 27 (Fig. 1C) is obtained by interpolation between January 21 and April 10.

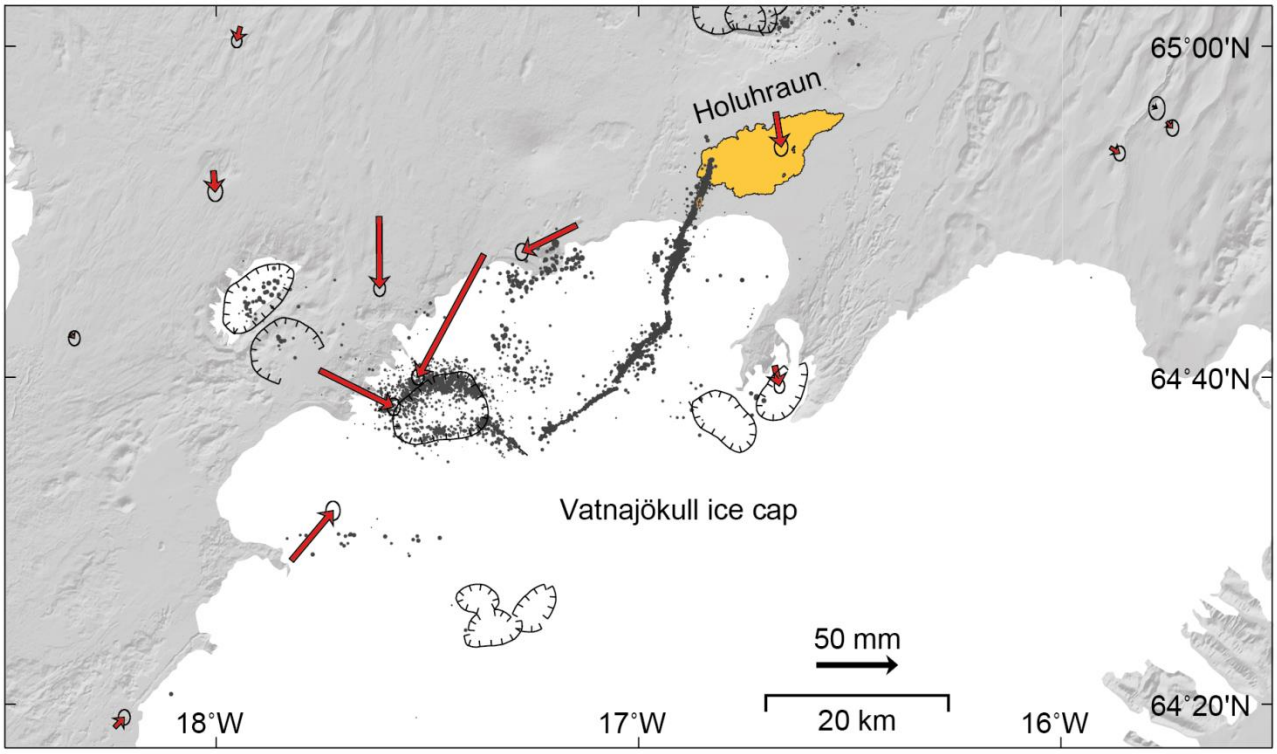

Fig. S3

GPS co-eruptive displacements, spanning September 21, 2014 until February 27, 2015, after the period of dyke opening had ended. The displacement field during the eruption shows consistent movements toward Bárdarbunga caldera suggesting deflation below the caldera. No other major deformation source can be observed during the eruption that can account for significant volume changes. Dots show relatively located earthquakes (20, 24).

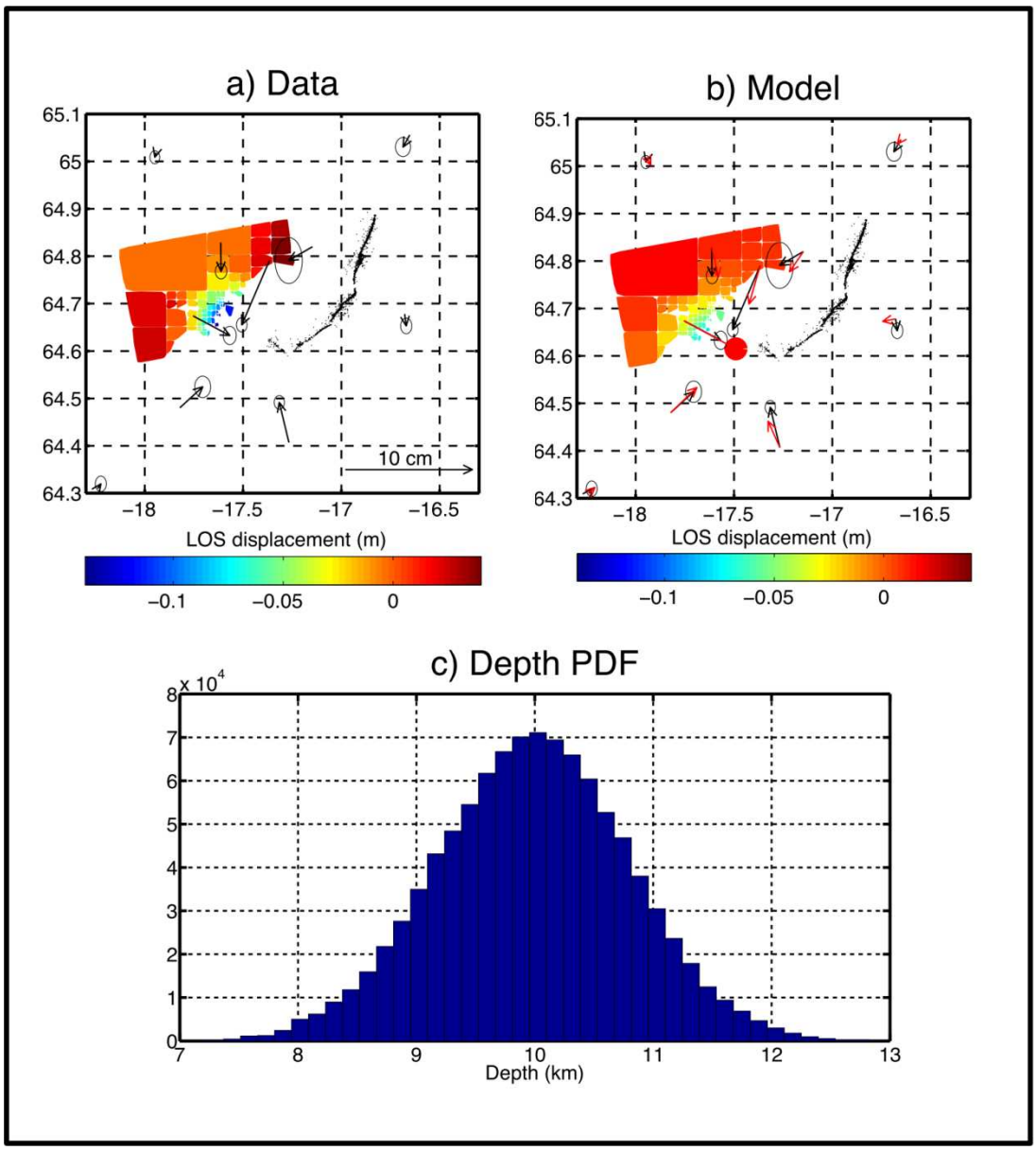

Fig. S4

Geodetic model of regional deformation using a contracting point pressure source. The upper panel from left to right displays the input data (a) and model (b). GPS data in both panels and the CSK ascending interferogram in (a) span the period September 16 to November 7, 2014. The red circle in (b) shows the location of the point pressure source. The black dots represent the seismicity in the vicinity of the dike. The black lines are the inferred dike location. The lower figure (C) displays the probability distribution for depth of the point source from 1 million iterations, using a Markov chain Monte Carlo approach.

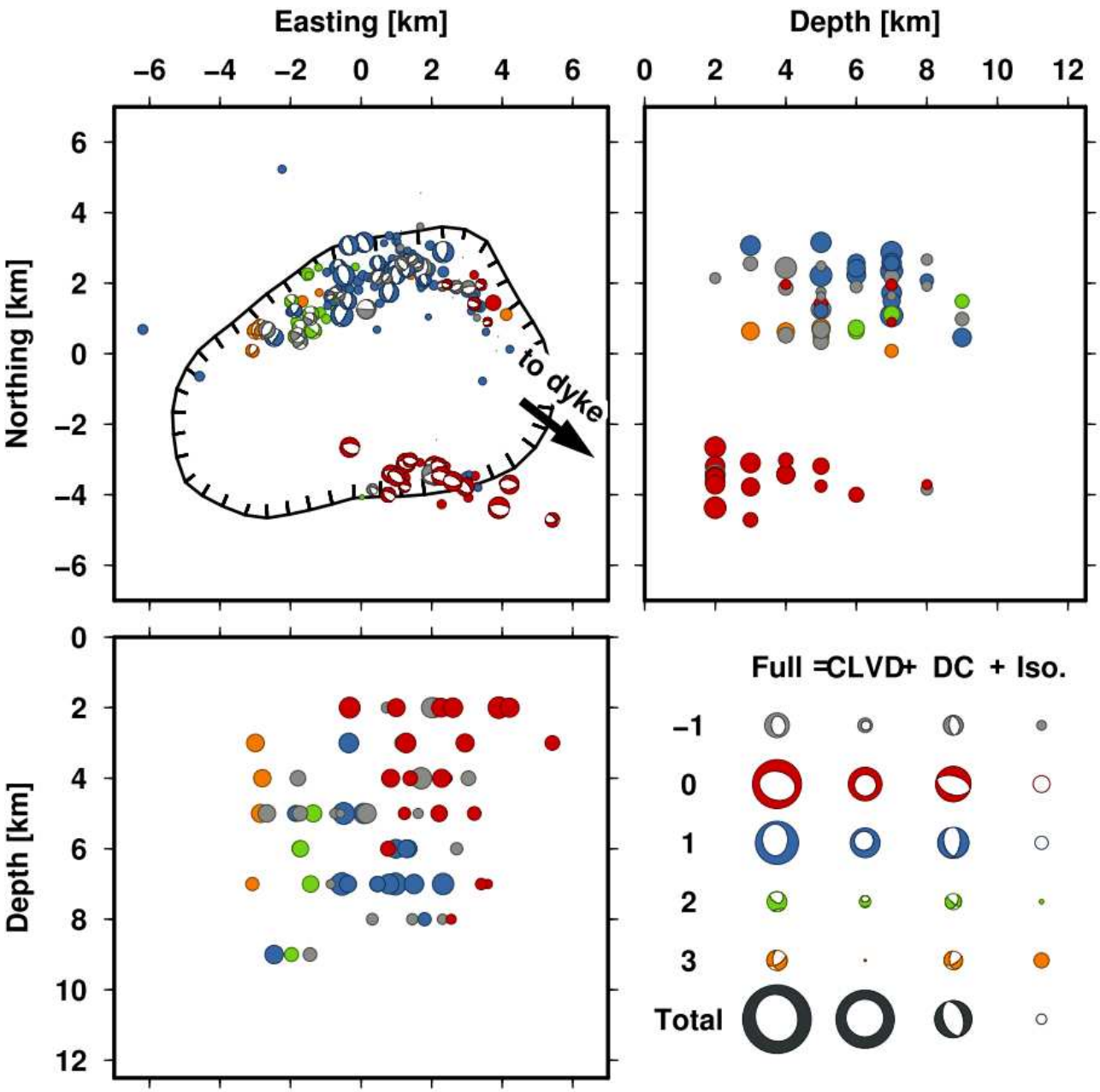

Fig. S5

Source mechanisms of 77 M>5 events. Double couple (DC) components of the retrieved moment tensors (top left) and centroid locations for different cross sections (top right, bottom left). Focal mechanisms are colored according to the result of a DC clustering. The two main clusters are the red cluster, with a WNW-ESE normal faulting component, dominant at the southern rim; and the blue cluster, with N-S oriented normal faulting, characteristic of the northern rim. The standard decomposition is given in the bottom right panel for the four clusters, un-clustered (grey) and cumulative MTs (black).

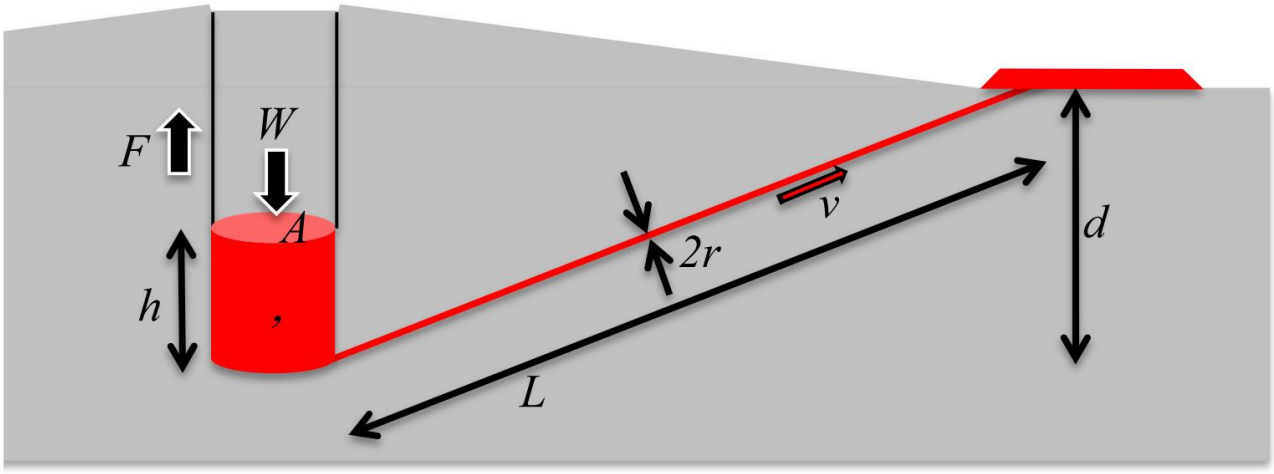

Fig. S6

Schematic of "piston collapse" model. Symbols as described in Materials and Methods

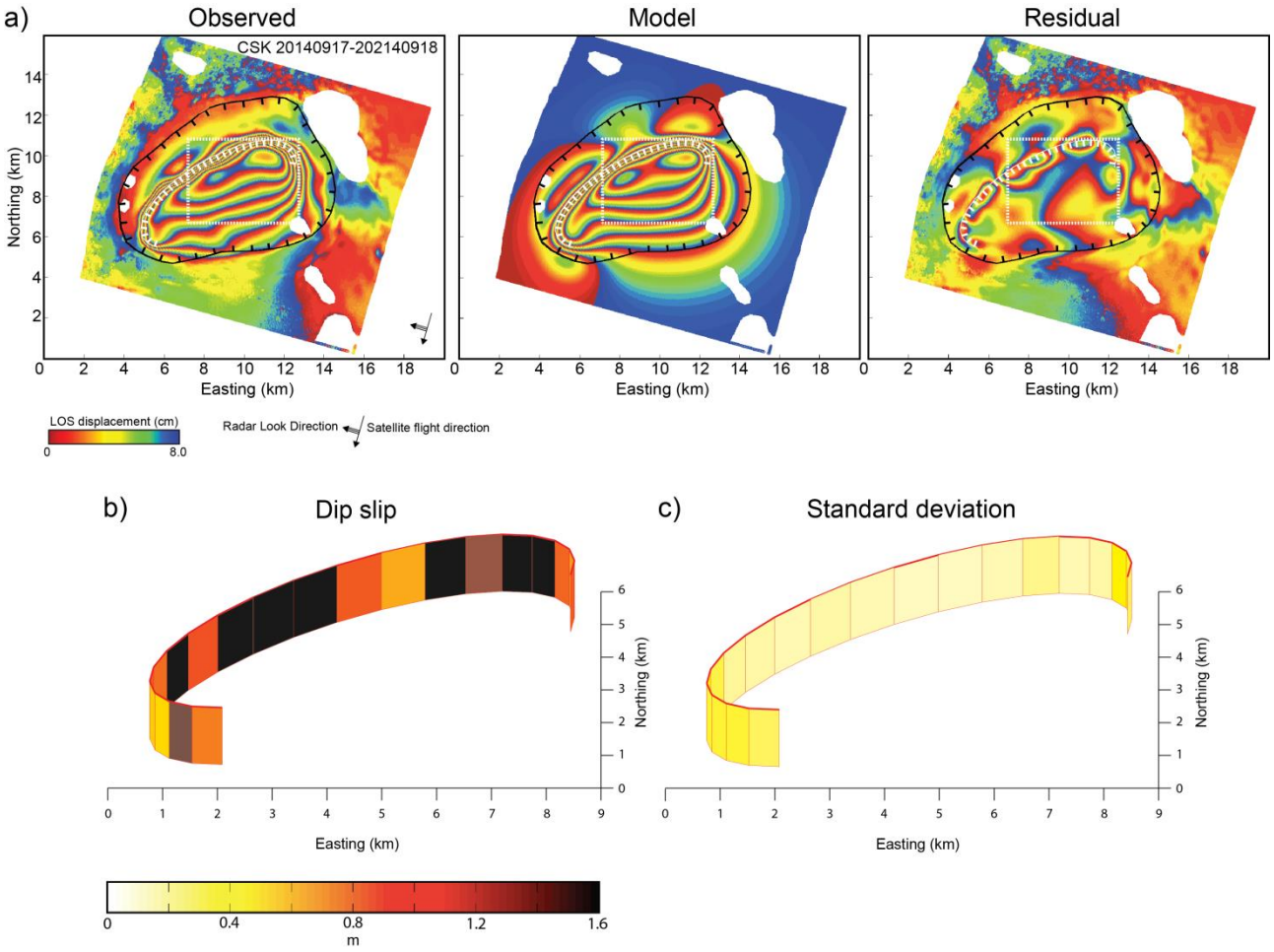

Fig. S7

Fault model for one-day interferogram. The data were acquired by COSMO-SkyMed constellation on 20140917 and 20140918. a) Comparison between observed, predicted and residual surface displacements. The black line outlines the outer caldera rim. The white lines mark the location of the inferred intra-caldera fault system (solid) and of the contracting body (dotted). As no slip is detected on the southern fault in the 24-hour period covered by the interferogram, the southern fault location is not constrained. Cauldrons, for which topography was not well constrained, are masked. b) Median of the posterior probability distribution of dip-slip on vertical fault segments, inferred from modelling. Color indicates the magnitude of slip. c) Standard deviation of the posterior probability distribution, using the same color scale as in b).

Fig. S8

Caldera-dike seismicity correlation. a) Geometry of correlated caldera-dike earthquakes. The dots show all dike earthquakes less than 2.5 km from the dike central line used for Figure 4a. b) Statistics of caldera-dyke earthquake correlations. Rate of dike earthquakes of magnitude $M \geq 0.8$ in time intervals shortly before and after large caldera earthquakes, of size ≥ 4.6, compared with the rate in reference intervals, consisting of all times during the respective period which are at least 3 hours before and at least 3 hours after all $M \geq 4.0$ caldera earthquakes. c) An example of how data was chosen for the analysis (randomly chosen 3 days in October). Upper panel: caldera earthquakes M>4. Lower panel: dike earthquakes during the same period. Blue bins mark three hours before and after caldera earthquakes with M>4.5 used in the study. Yellow bins

1098 show data between significant (M>4) caldera earthquakes, used to estimate background seismicity in the
1099 dike. Pink shaded bins show data that were not used in the analysis (due to possible overlapping effects).

1100

1101

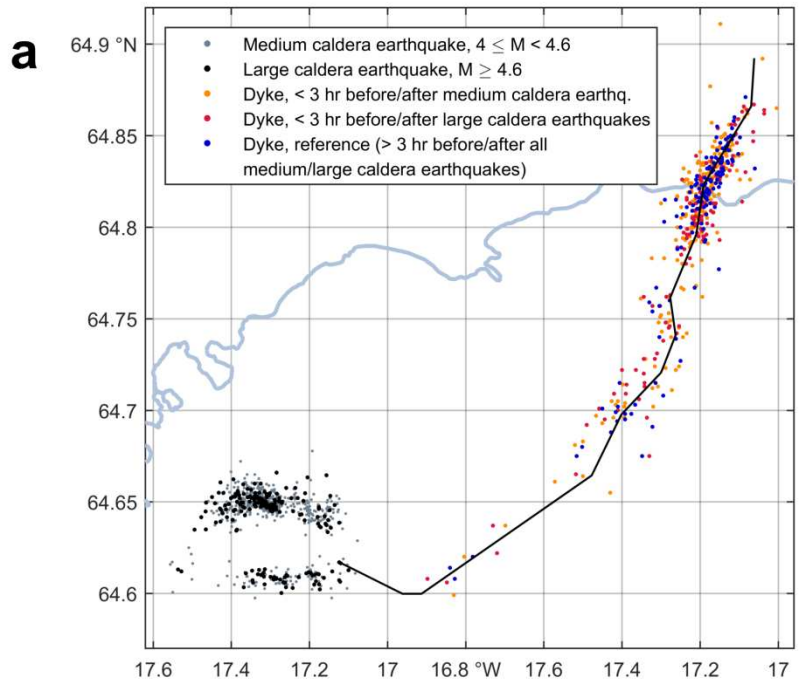

b

Period (2014)	Reference time, total days	Reference rate in dyke (earthq./hr.)	No. of M ≥ 4.6 earthquakes in caldera	Intervals 0–3 hours before M ≥ 4.6 caldera earthquakes: Total hours	No. of eq. in dyke	Rate (eq./hr.)	Intervals 0–3 hours after M ≥ 4.6 caldera earthquakes: Total hours	No. of eq. in dyke	Rate (eq./hr.)
01–06 Sept.	3.1	7.04	8	19	132	6.85	19	140	7.26
07–12 Sept.	2.6	2.58	11	30	66	2.20	30	67	2.23
13–18 Sept.	3.1	1.39	9	21	30	1.40	21	27	1.26
19–24 Sept.	2.6	0.85	10	28	26	0.94	28	21	0.76
25–30 Sept.	1.3	0.47	10	29	23	0.81	29	20	0.70
Oct. 2014	5.0	0.14	74	179	44	0.25	179	47	0.26
Nov. 2014	4.2	0.14	25	64	19	0.30	64	12	0.19
Dec. 2014	11.0	0.09	15	42	5	0.12	42	3	0.07
Jan. 2015	14.8	0.19	13	39	10	0.26	39	9	0.23
1–21 Feb. 2015	18.6	0.10	3	9	1	0.11	9	3	0.33